ANNUAL REVIEWS

Annual Review of Biochemistry

Current Understanding of the Mechanism of Water Oxidation in Photosystem II and Its Relation to XFEL Data

Nicholas Cox,[1] Dimitrios A. Pantazis,[2] and Wolfgang Lubitz[3]

[1]Research School of Chemistry, The Australian National University, Canberra ACT 2601, Australia; email: nick.cox@anu.edu.au

[2]Max-Planck-Institut für Kohlenforschung, 45470 Mülheim an der Ruhr, Germany; email: dimitrios.pantazis@kofo.mpg.de

[3]Max-Planck-Institut für Chemische Energiekonversion, 45470 Mülheim an der Ruhr, Germany; email: wolfgang.lubitz@cec.mpg.de

Annu. Rev. Biochem. 2020. 89:795–820

First published as a Review in Advance on March 24, 2020

The *Annual Review of Biochemistry* is online at biochem.annualreviews.org

https://doi.org/10.1146/annurev-biochem-011520-104801

Keywords

oxygen-evolving complex in PS II, spectroscopy, X-ray crystallography, X-ray free-electron laser, XFEL, quantum chemical calculations, water oxidation mechanism

Abstract

The investigation of water oxidation in photosynthesis has remained a central topic in biochemical research for the last few decades due to the importance of this catalytic process for technological applications. Significant progress has been made following the 2011 report of a high-resolution X-ray crystallographic structure resolving the site of catalysis, a protein-bound Mn_4CaO_x complex, which passes through ≥ 5 intermediate states in the water-splitting cycle. Spectroscopic techniques complemented by quantum chemical calculations aided in understanding the electronic structure of the cofactor in all (detectable) states of the enzymatic process. Together with isotope labeling, these techniques also revealed the binding of the two substrate water molecules to the cluster. These results are described in the context of recent progress using X-ray crystallography with free-electron lasers on these intermediates. The data are instrumental for developing a model for the biological water oxidation cycle.

Contents

1. INTRODUCTION

Oxygenic photosynthesis: process performed by cyanobacteria, algae, and plants to split water, release oxygen, and reduce CO_2 to carbohydrates

XFEL: X-ray diffraction with free-electron lasers

PS I, PS II: photosystems I and II are the reaction centers of oxygenic photosynthesis in which light-induced charge separation and subsequent electron transport take place

OEC: oxygen-evolving complex harbored in the membrane protein called photosystem II, a manganese-calcium cluster

Oxygenic photosynthesis, performed by cyanobacteria, algae, and plants, is the largest and arguably the most important chemical process on Earth. It stores the energy of the sun in chemical compounds (carbohydrates) by reduction of atmospheric carbon dioxide (CO_2). The reducing equivalents (electrons) required for this reaction are derived from the oxidation of water, an abundant material. This chemically challenging process was developed only once in biology, about 2.5 billion years ago. Water oxidation and dioxygen (O_2) release resulted in our O_2-rich atmosphere, the ozone layer, and eventually the evolution of multicellular lifeforms (1, 2). A detailed understanding of how nature uses sunlight to split water and store energy provides a blueprint for future technologies based on using solar energy to satisfy mankind's ever-increasing energy demands (3–13).

In this short review, the principles of photosynthetic water oxidation are described, with special emphasis on the recent data obtained from X-ray diffraction with free-electron lasers (XFEL) and results obtained from advanced spectroscopic techniques in combination with quantum chemical calculations. Oxygenic photosynthesis, photosystem II, and water oxidation have been authoritatively reviewed in recent years, and the reader is referred to References 14–20 for further details.

2. BASIC FUNCTION OF WATER OXIDATION IN PHOTOSYNTHESIS

The light-induced oxidation of water occurs in the transmembrane protein complex called photosystem II (PS II) (21) (**Figure 1*a***). After four light-absorption (hν) and single-charge separation events, one O_2 molecule is formed and released (22):

$$2H_2O \xrightarrow{4h\nu} O_2 + 4e^- + 4H^+. \quad 1.$$

PS II harbors a protein-bound, oxygen-bridged tetranuclear manganese/calcium cluster, Mn_4CaO_x (**Figure 1*b*,*c***), the water-oxidizing complex or oxygen-evolving complex (OEC). The OEC is linked to the photo-induced electron transport chain by a redox-active tyrosine residue

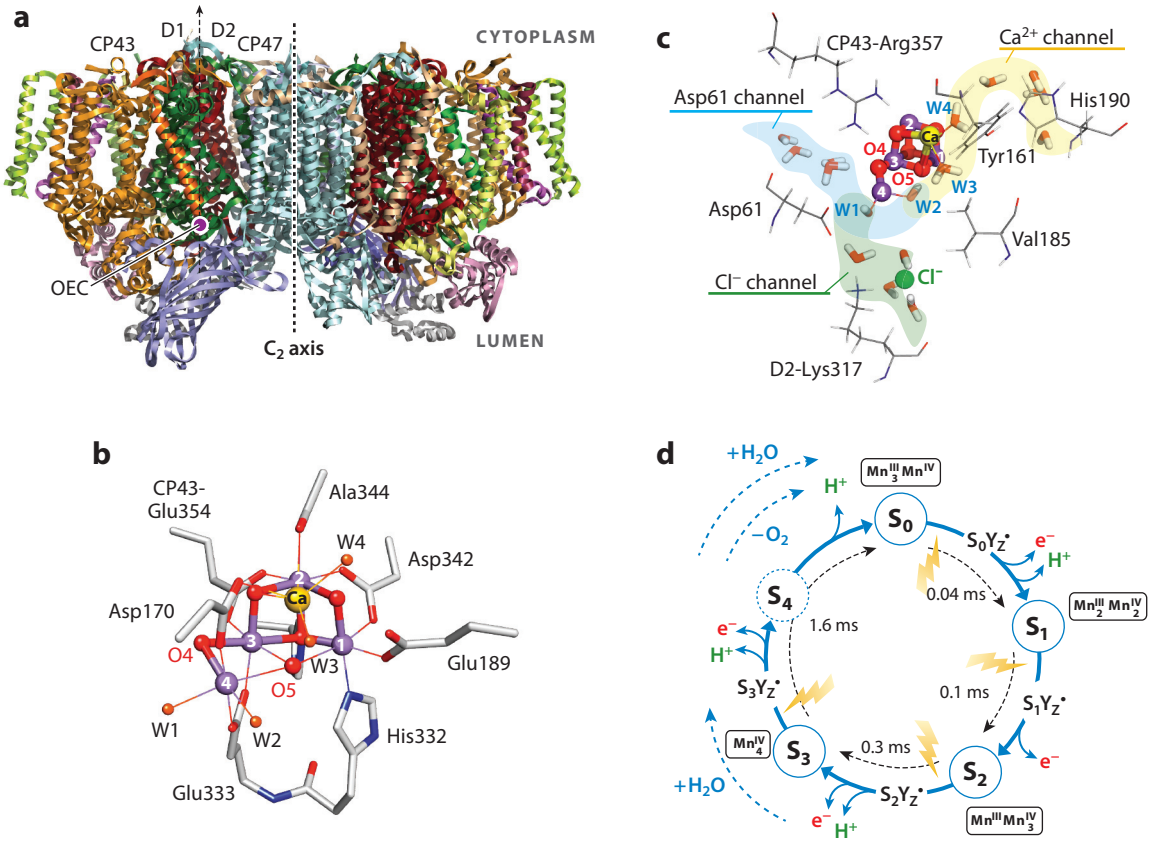

Figure 1

(*a*) X-ray crystallographic structure of PS II from *Thermosynechococcus vulcanus* (46). The dimeric membrane protein (≈700 kDa) is related by a C_2 axis. Major protein subunits and the location of the oxygen-evolving complex (OEC) in the D1 protein (*dark green*) are shown. (*b*) Mn_4CaO_5 cluster constituting the OEC with its amino acid surrounding and the bound water molecules (W1 to W4). The four Mn ions (*purple*) are numbered, and Ca (*yellow*) and O4 and O5 (*red*) are indicated. (*c*) Water channels leading to the OEC (46), which could be multifunctional (e.g., proton transfer). The positions of the redox-active tyrosine (Y_Z) (D1-Y161) and the essential Cl^- ion are also shown. (*d*) Water oxidation (Kok) cycle (23) showing the five basic S states (S_0 to S_4), the light-induced one-electron oxidation steps (involving Y_Z), the proton and oxygen release, and the uptake of the two substrate water molecules. The Mn oxidation states (82) and the reaction times (25) are also given.

(Y_Z). The four oxidizing equivalents for the water-oxidation reaction are stored transiently in the manganese cluster (23). Thereby, the OEC passes through five states (S_0 to S_4), which differ by the number of oxidizing equivalents transiently stored in the cofactor, indicated by their subscript (**Figure 1*d***). In this cycle, S_0 to S_3 can be trapped and studied, whereas S_4 is transient and has not been directly observed so far with O_2 released in a concerted reaction with an equilibrium constant of $K > 1.0 \times 10^7$ (24) (**Figure 1*d***). The kinetics of the proton release, which follows a 1:0:1:2 pattern (or 1:0:1:1:1), has been determined (25–29). Measurements showed that the reaction times for the different steps of the cycle lie in the micro- to millisecond range (40 μs to 1.6 ms) (**Figure 1*d***) (25). Thus, the OEC turns over in about 2 ms, although the turnover of the complete PS II takes about 10 ms due to the slower electron acceptor site kinetics (17). The lifetime of intact PS II is only about 30 min under normal light, which is caused by the harsh conditions necessary to oxidize water in PS II. As a result, there is an efficient repair mechanism for the affected protein

S_0 to S_4: states of the water-splitting cycle

scaffold (**Figure 1*a***) to overcome this otherwise serious degradation problem (30–32). The time for repair of the full system has been estimated at less than 1 h (33).

There are several interlinked reasons why the Mn_4CaO_x cluster functions in the way outlined above (34). First, the Mn cluster acts as an interface and storage device between the very fast light reaction (picosecond timescale) and the slow four-electron water oxidation chemistry (millisecond timescale), bridging a kinetic gap of nine orders of magnitude. Second, the energetic cost is significantly lowered by first storing oxidizing equivalents and then performing the four-electron chemistry. Third, proton release during charge accumulation leads to charge neutrality so that about the same oxidizing potential can be used for all Mn oxidation events. Finally, this sequence avoids the formation of reactive oxygen species as intermediates resulting from partial oxidation of substrate water, which are highly reactive and would destroy the protein. However, even by these measures, PS II is not fully protected against deleterious species occurring from time to time in the antennae and/or reaction center (RC) of PS II. The major problem is the chlorophyll triplet states that react with the released triplet oxygen to produce highly reactive singlet oxygen, which destroys pigments and protein (35).

RC: reaction center

XRD: X-ray diffraction

EXAFS: extended X-ray absorption fine structure

EPR: electron paramagnetic resonance; magnetic resonance technique performed to characterize paramagnetic substances

ENDOR: electron nuclear double resonance; technique to resolve the hyperfine interaction between unpaired electron and nuclear spins obtaining spin density distributions

3. DETERMINATION OF THE CRYSTALLOGRAPHIC STRUCTURE OF PHOTOSYSTEM II

3.1. Photosystem II Crystallization and X-Ray Diffraction

It took almost two decades after the crystallization of the first membrane protein, the bacterial photosynthetic RC (36), until structures of PS I (37) and PS II (38) were reported in 2001 by the groups of Horst T. Witt and Wolfram Saenger in Berlin (for a timeline, see **Figure 2**). The photosystems were purified from the thermophilic cyanobacterium *Synechococcus elongatus* (later renamed *Thermosynechococcus elongatus*). For PS II, a structure with 3.8 Å resolution was obtained (38). This first crystallographic structure provided valuable insight into the arrangement of the protein subunits and the cofactors of PS II. In particular, it demonstrated that the OEC and Y_Z do not form a single complex but are spaced 7 Å apart, excluding the popular hydrogen atom abstraction model for O–O bond formation (39). This structure, however, was of insufficient resolution and did not allow the positions of the atoms in the OEC to be determined. In part this was traced back to radiation damage induced by the intense X-ray beam used for X-ray diffraction (XRD) data collection in modern synchrotrons using small, single crystals. All synchrotron structures described below suffer from this problem. X-ray absorption spectroscopy experiments with varying beam intensity conducted by the groups of Yano (40) and Dau (41) have shown photoreduction of the oxidized Mn ions (reduction to Mn^{2+}), which leads to perturbation and ultimately disintegration of the complex and blurring of the electron density associated with the cluster.

In 2004, the group of James Barber (42) (Imperial College London) presented an improved structure of PS II from *T. elongatus* at 3.5 Å resolution. Based on their refined data, including anomalous diffraction to identify the Ca, previous extended X-ray absorption fine structure (EXAFS) (43), and electron paramagnetic resonance (EPR)/electron nuclear double resonance (ENDOR) data (44, 45), the authors proposed a heterometallic cubane-type structure for the OEC, which contained an oxo-bridged Mn_3CaO_4 unit linked to a more distant fourth Mn ion. This model—although not entirely correct in all details (oxygen bridges, amino acid ligands, etc.)—was the first to correctly predict the basic cubane-type structure of the Mn/Ca cluster with a dangling Mn.

In the following years, several groups were working on the apparent problems encountered with XRD structure determinations of large membrane proteins like PS II. The challenges included (*a*) improved resolution, (*b*) minimization of radiation damage, (*c*) preparation of large

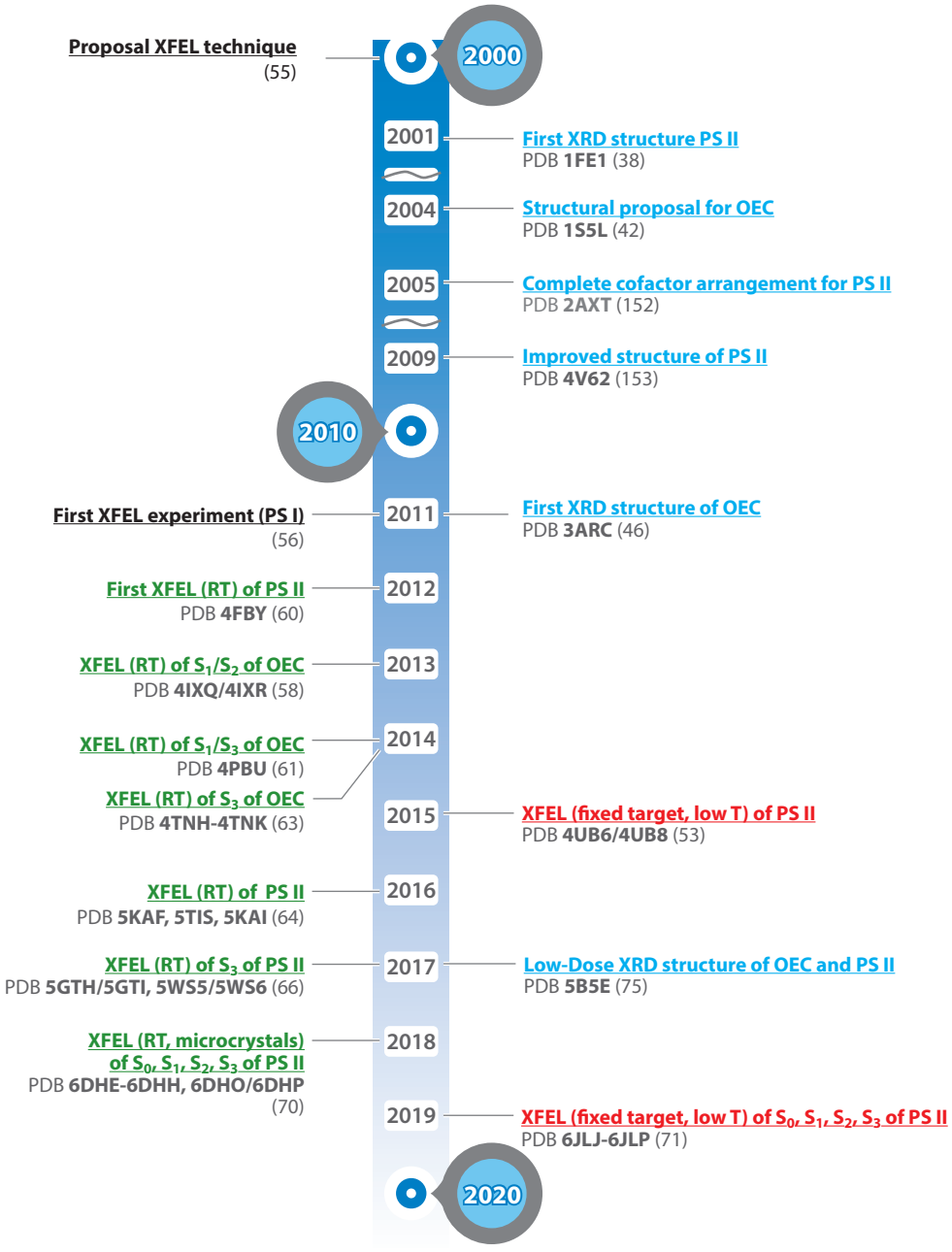

Figure 2

Milestones in the determination of the structure of photosystem II (PS II) and the oxygen-evolving complex (OEC) using (classical) X-ray diffraction (XRD) and X-ray crystallography with free-electron laser (XFEL) techniques (38, 42, 46, 53, 55, 56, 58, 60, 61, 63, 64, 66, 70, 71, 75, 152, 153). Shown are low-temperature XRD (*blue*) and XFEL (*red*) structures and XFEL structures using jet injection of microcrystals at room temperature (RT; *green*). In the latest structures, resolutions close to 2.0 Å (XFEL) and below 1.9 Å (XRD) were obtained.

crystals with well-defined specific catalytic states, (*d*) room temperature, and (*e*) time-resolved experiments. A remarkable breakthrough was obtained for PS II in 2011 by the groups of Jian-Ren Shen (Okayama, Japan) and Nobuo Kamiya (Osaka, Japan) (46), who published a greatly improved structure from *Thermosynechococcus vulcanus* at 1.9 Å resolution, in which the atomic arrangement of the ions in the OEC could finally be resolved. The structure depicted in **Figure 1*b*** shows the Mn_4CaO_5 cluster, with three Mn (Mn1 to Mn3), one Ca, and four (bridging) oxygens forming an asymmetric cubane-like structure. The fourth Mn (Mn4) is located outside the cluster and linked by two oxygens (O4 and O5) forming μ-oxo bridges. The distances between the five metal centers were largely in agreement with those determined earlier from EXAFS studies (47, 48), taking into account a coordinates error of 0.16 Å in the crystal structure. Four water molecules (W1 to W4) were shown to be associated with the Mn_4CaO_5 cluster, with two bound to Mn4 and two to the Ca, suggesting that these may serve as substrates for water oxidation (**Figure 1*b***). Furthermore, all amino acid residues associated with the cluster could finally be identified. Together with the oxo-bridges and the water molecules, this led to a saturating ligand environment of the metal ions (each Mn has six ligands, and Ca has seven). Information about Y_Z, the hydrogen bond network, charge balance, the second coordination sphere, the chloride cofactor binding, and possible proton (and water) channels has also been provided in this work (**Figure 1*c***). Umena et al. (46) claimed that the structure was obtained from dark-stable PS II (S_1 state of the OEC). This has been challenged by various researchers, since some of the observed distances [in particular the binding of one oxygen bridge (O5)] were recognized as being too long. Several subsequent theoretical studies showed that the actual oxidation state of the OEC in this structure was probably a mixture of overreduced states not present in the catalytic cycle (49–51), which posed some basic problems for the OEC structure.

To overcome the problems of XRD mentioned above, the Shen group tried to obtain a high-resolution structure with reduced radiation damage using femtosecond pulsed X ray crystallography with XFEL, vide infra. They used a large single crystal in which the position of the beam could be changed (scanned) over the entire size (surface) of the crystal (52). The related work on PS II, which was published early in 2015 (53), obtained a resolution of 1.95 Å (at cryogenic temperatures) and allowed a detailed comparison with the earlier structure (46), both obtained from *T. vulcanus* (for a discussion, see 54). The obtained differences were not large, and thus the problem posed by quantum chemical calculations, which predicted a significant movement of the position of O5 (see **Figure 5**), could not be fully resolved by this approach.

3.2. Structural Refinement of Photosystem II Using X-Ray Free-Electron Lasers

The use of the very intense femtosecond X-ray pulses from free electron lasers to obtain crystallographic structures was first proposed by Neutze et al. (55) in 2000 (see **Figure 2**). The authors postulated that this approach could be used to obtain diffraction patterns for a protein prior to its obliteration, which was called "diffract before destroy" (or "probe before destroy"). It took about 10 years before it was shown by Chapman, Fromme, and colleagues (56) in a ground breaking paper that diffraction patterns can indeed be obtained, even from complex photosynthetic (membrane) proteins.

Since the XFEL pulses are extremely intense ($\geq 10^9$ times brighter than the best modern synchrotrons), the crystals are destroyed and must be replaced after each shot. This requires measurements of multiple small crystals with high throughput or, alternatively, of a large crystal on which the pulsed beam position is changed. In the latter approach, a fixed target (large crystal or embedded microcrystals in a film) on a translational stage is used to perform the XFEL experiment (52, 53), which can be done at variable temperatures and allows for direct comparison with

the classical XRD experiment at low temperatures with comparable resolution (see 53, figure 2). Another approach involves jet-injection of nanocrystals as a liquid or aerosol into the beam at room temperature, e.g., as lipidic cubic phase (57). The complete diffraction pattern is then obtained by serial injection and processing of a very large number of crystals. Due to the random orientation of the crystals and differing intensity of the X-ray pulses in each shot, special detectors and massive data postprocessing are required. The technique is called serial femtosecond X-ray crystallography with a free-electron laser (SFX).

SFX: serial femtosecond X-ray crystallography with a free-electron laser

The advantages of SFX include (*a*) limited or no radiation damage, since the measurement is completed within a few femtoseconds, i.e., before photochemistry in the crystal can take place; (*b*) that only very small crystals are necessary to obtain a diffraction pattern; (*c*) that data can be collected at room temperature under physiological conditions; and (*d*) time resolution on timescales shorter than Laue diffraction experiments.

The XFEL technique can be combined with methods to prepare a specific state on a short timescale (microseconds to milliseconds) by either light or rapid mixing before the diffraction experiment. It can also be combined with spectroscopic measurements (e.g., X-ray emission spectroscopy) on the jet of crystals at room temperature (58, 59) to probe the electronic state of the object studied. SFX is particularly useful for studying intermediates in enzymatic reactions under physiological conditions to achieve a better understanding of the catalytic mechanisms. In the case of PS II, the OEC can be advanced by 1–3 light/laser flashes prior to the experiment to obtain the appropriate S state (see **Figure 1*d***), followed by the hard X-ray pulse to obtain the diffraction pattern. This offers the unique possibility to obtain the structures of all (meta)stable states of the water-splitting cycle. One problem is the yield of the different states in the repetitive flash experiments, i.e., the contamination of a targeted S state by other unwanted S states. This could lead to difficulties in structure determination even in cases with sufficient resolution, which is a general problem in XFEL experiments. Furthermore, it is not clear whether a certain state that can exist in different conformations will show all these forms under the specific conditions of the experiment at the chosen temperature.

The first protein crystal structure determined using SFX on PS I, in which a resolution of 8.7 Å was obtained, was reported in 2011 (56). In 2012, Kern et al. (60) were the first to show that SFX is also possible on PS II microcrystals at room temperature (resolution 6.5 Å). Subsequent work by the same group examined the OEC in the S_1 (dark) and S_2 (one flash advanced) states at room temperature (resolutions 4.1 Å and 5.7 Å, respectively) (58) and showed no major structural changes in the S_1 to S_2 transition of the OEC. Experiments on S_3, the state directly prior to O–O bond formation in the cycle, generated great interest. Employing two lasers for progressively exciting the OEC from S_1 to S_3 (double flash), Fromme and colleagues (61) collected data on dark and illuminated microcrystals and compared the electron densities, albeit with limited resolution (5 Å for dark and 5.5 Å for light). The data analysis yielded differences between S_1 and S_3 that were interpreted as an elongation of the bonding between the dangling Mn4 and the cubane Mn_3CaO_x structure, with concomitant changes of some protein loops. It was speculated that this could allow the cluster to bind the second substrate water in the S_2 to S_3 transition (61). Based on these results, the electron density of the cofactor was successfully modeled by inclusion of an additional water-derived ligand by the groups of Brudvig and Batista (62). However, concurrent SFX studies by Kern et al. (63) (4.2–5.2 Å resolution) and also later by Young et al. (64) with better resolution (≈3.0 Å) did not observe any of the changes reported by the Fromme group (see also 65).

The situation changed in 2017 when the Shen group (66) published a SFX paper on the S_3 state at a higher resolution of 2.35 Å, in which significant structural changes were observed, culminating in the detection of the insertion of a sixth oxygen (O6) in close proximity to O5 in the quasi-center of Mn1 and Mn4 in the OEC (see **Figure 3*a***). The O5–O6 distance was found to be very short

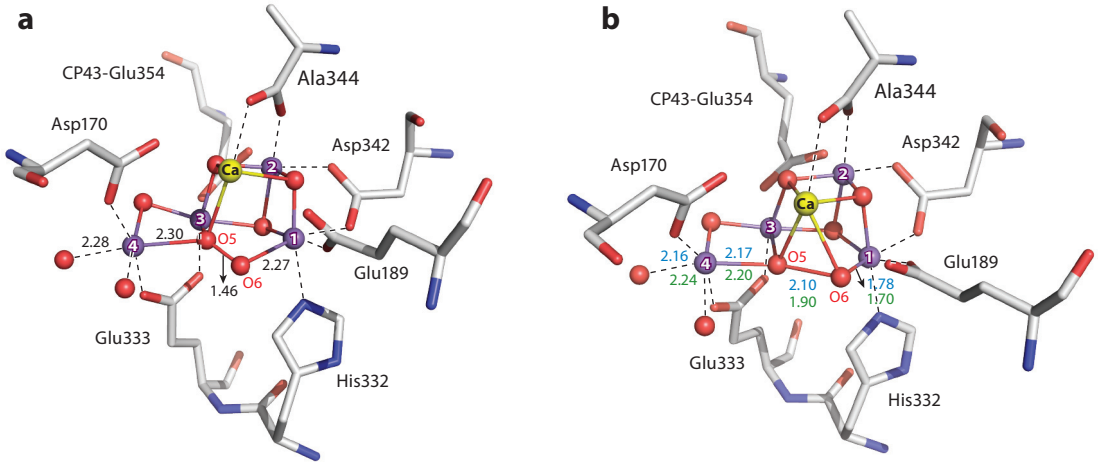

Figure 3

Models of the S_3 state of the oxygen-evolving complex obtained from serial femtosecond X-ray crystallography with a free-electron laser. Panel *a* shows the model from Suga et al. (66), and panel *b* shows the model from Kern et al. (70) (distances in *blue*) and Suga et al. (71) (distances in *green*). Selected distances are given in angstroms. In the most recent structure by Suga et al. (71), the distance between O5 and O6 is 1.9 Å, whereas in the Kern et al. (70) study, the structure is 2.1 Å. Figure adapted from Reference 67.

(≈1.5 Å), suggesting that these oxygens represent the two substrates of the reaction and that this is the site of O_2 formation and release. Furthermore, a rearrangement of water molecules near the OEC and in the hydrogen bond network important for proton transfer was detected. The short O5–O6 distance was interpreted as indicating the onset of O–O bond formation (peroxide or superoxide) already in the S_3 state (67) (**Figure 3*a***). This possibility, however, had been excluded in earlier spectroscopic experiments (68, 69) and thus caused extensive discussions in the literature [reviewed by Pantazis (67)]. However, more recent, higher-resolution measurements described below show that O–O bond formation has not yet occurred in the S_3 state (see **Figure 3*b***).

The most recent SFX structures of the OEC poised in the S_3 state were published late in 2018 by Kern et al. (70) and in 2019 by Shen and colleagues (71). In both studies, all (meta)stable states of the Kok cycle, S_0, S_1, S_2, and S_3, were reported with very good resolution (close to 2Å). Both groups now observe the insertion of a new water-derived ligand in the S_3 state. In Kern et al. (70), this oxygen is referred to as Ox instead of O6. For simplicity, we refer to this oxygen as O6. The position of O6 is different from that obtained in the original Suga et al. structure (66) (see comparison in **Figure 3**). Importantly, the much longer distance between O5 and O6 (2.1 Å and 1.9 Å in the two studies, respectively) excludes peroxo bond formation in S_3. The authors of both studies suggested that O6 could serve as the second substrate forming O_2 with O5—or it serves to refill the O5 position in the following cycle. In both cases, it was suggested that O6 represents W3 in the preceding S_2 state structure (i.e., that water accesses this site via the Ca channel; see **Figure 1*c***). To facilitate this process, it has been suggested that Glu189, a bridging ligand between Ca and Mn1, rotates out of the way. A small change in the Glu189–Ca bond length (0.5 Å) is resolved in the S_3 structure, which could indicate the larger (>2 Å) conformation change that is needed for this process to occur (see **Figure 3**). The protonation state of O6 cannot be directly determined; in both structures, it is modeled as bridging the Mn1 and Ca. Kern et al. (70) prefer to assign O6 as a terminal OH, which potentially H bonds to one of the carboxylate oxygens of Glu189. Suga et al. (71) also assign an H bond between Glu189 and O6 but instead prefer the Glu189 being protonated with O6, representing a terminal oxo ligand. The terminal

Kok cycle or S state cycle: catalytic cycle of water splitting (oxidation) by light performed by the oxygen-evolving complex in photosystem II

oxo is described as having some oxyl character, suggesting a radical coupling O–O bond formation mechanism between the oxo (O5) and the oxyl (O6); for further discussion, see Section 4.1. The Glu189–O6 distance (2.9 Å) in the new Suga et al. (71) structure is consistent with an H bond distance, whereas the same distance in the Kern et al. (70) structure (2.5 Å) is arguably too short for an H bond.

XANES: X-ray absorption near edge structure

In summary, it can be stated that the quality of the SFX data on PS II and the OEC has made enormous progress during the last few years and that structural models of the S_3 state are converging. In our opinion, however, there are two issues with current SFX data that need to be considered when discussing the finer details of the cofactor. First, in the two current SFX structures, metal–ligand bond lengths remain very similar in all S states for Mn ions that undergo oxidation (70). This is best observed for the terminal Mn4 ion, whose ligand field resembles that of an octahedral Jahn–Teller distorted Mn^{III} ion. In all chemical models of the S state cycle, the Mn4 ion obtains the +IV oxidation state level in the S_2 and S_3 state, and therefore the bond length should change. Second, in the two current SFX structures, the bond lengths for the inserted water-derived ligand O6 in the S_3 state display short bond lengths and bond angles outside those observed in model systems (72, 73).

The origin of these chemical inconsistencies is unclear at present. It is well documented in the XRD literature that it is difficult to accurately resolve the positions of light atoms near metal centers; in the case of the FeMoco cofactor of nitrogenase, the central carbon atom of the structure was only clearly resolved in structures with a resolution of less than 1 Å (74). As described above, in the case of the S state cycle there is the added complication of state scrambling due to incomplete advancement and potentially the presence of more than one S state conformer (see Section 4.2). An important consequence is that for all S_3 state structures, there is incomplete occupancy of O6 hampering its clear detection, which may introduce uncertainty in its position.

4. SPECTROSCOPIC INFORMATION ON THE OXYGEN-EVOLVING COMPLEX

Although crystallographic measurements have made extraordinary progress over the last decade, their interpretation is still heavily dependent on complementary spectroscopies. Importantly, crystallographic measurements of metallocofactors are unable to determine metal oxidation and protonation states, spin states, and to some extent protein dynamics. And in this instance, crystallography cannot unambiguously assign the two substrate waters of the reaction. A brief description of complementary spectroscopic data that provide this information is given below.

4.1. Mn Oxidation States in Each S State and Coupled Proton Release

With the exception of the S_1 state, where the Jahn–Teller axis of the two Mn^{III} ions (Mn1 and Mn4) can be observed (75), the oxidation states of the Mn ions in all other S states cannot be directly determined by crystallography. The net oxidation state of the S_2 state (and by inference, all S states) was first constrained in the early 1980s by EPR spectroscopy (76). The observation that the cofactor displayed a multiline EPR signal similar to that of mixed-valence, oxygen-bridged $Mn^{III}Mn^{IV}$ dimer complexes required that the cofactor be made up of Mn ions in the +III and +IV oxidation states and that the total number of valence electrons be odd (44, 45). This leads to only two possible configurations: $(Mn^{III})_3Mn^{IV}$, termed the low oxidation state model, or $(Mn^{IV})_3Mn^{III}$, termed the high oxidation state model. Subsequent X-ray absorption near edge structure (XANES) (77, 78) and EPR/ENDOR (79, 80) measurements, which both exclude a Mn^{II} ion in the reaction cycle, implicit in the low oxidation state model, demonstrated that the high oxidation state assignment

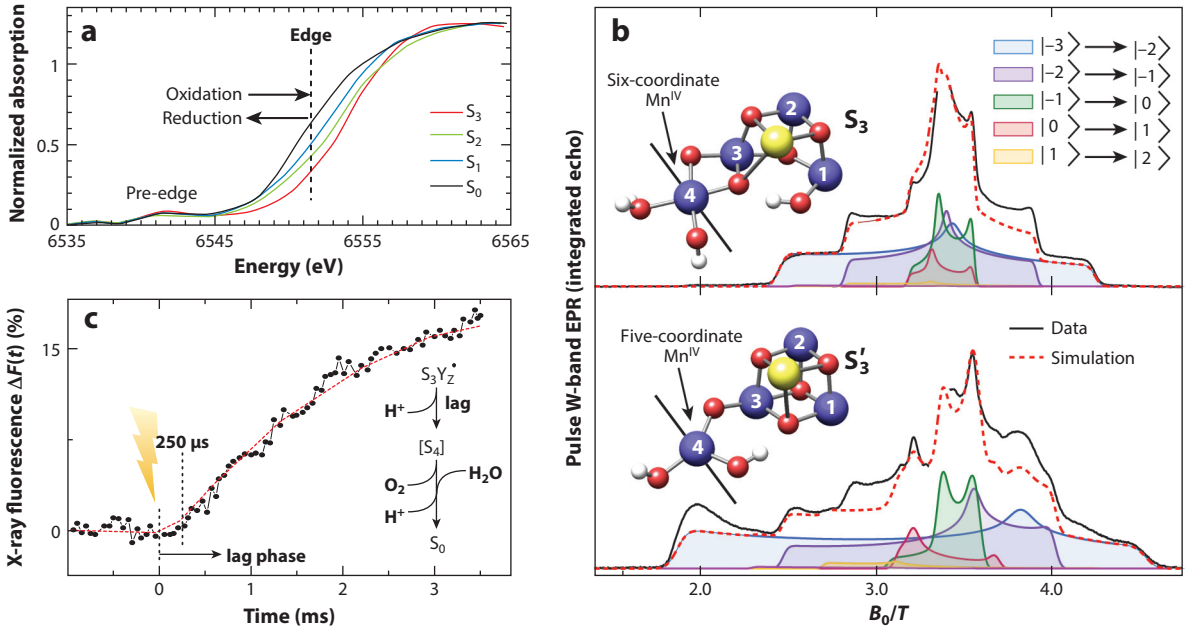

Figure 4

(*a*) X-ray absorption near edge structure spectroscopy of the Mn_4CaO_x cluster during the S state cycle (77, 78, 81). Oxidation of the Mn ions leads to a shift of the absorption edge to higher energy. Panel *a* adapted with permission from Reference 78. (*b*) The two forms of the S_3 state as visualized by high-field electron paramagnetic resonance (EPR) spectroscopy (69, 124). The width of the EPR signal correlates inversely with the net coordination number of the cofactor and can be benchmarked against model complexes. The narrower signal corresponds to the final S_3 form; it represents a complex containing only octahedral Mn^{IV} ions (69). The broader EPR signal corresponds to the precursor S_3 form (S_3'). Its larger width requires that it still contains a five-coordinate Mn^{IV} ion, most likely located at Mn4 (124). (*c*) X-ray fluorescence data showing the kinetics of the O–O bond formation step. This study shows that the first step (lag phase) of the reaction represents deprotonation of the cofactor, followed by the formation of the S_0 state with concomitant loss of the S_3 state. Panel *c* adapted with permission from Reference 87.

for S_2 is correct (see **Figure 1*d***). Thus, the net oxidation states of S_0, S_1, and S_2 are $(Mn^{III})_3Mn^{IV}$, $(Mn^{III})_2(Mn^{IV})_2$, and $(Mn^{IV})_3Mn^{III}$. Density functional theory modeling of all S states supports this assignment, reproducing key structural and magnetic constraints. This includes metal–metal distances derived from EXAFS and metal- and ligand-centered hyperfine couplings.

The Mn oxidation states of S_3 remained contentious for many years. Owing to the small shift of the XANES edge and K_β emission line (77) (**Figure 4*a***), it was proposed that either one of the ligands of the OEC, instead of one of the Mn ions, is oxidized upon moving from the S_2 to S_3 state (however, see 78). Recent high-field EPR data show that this is not the case (69), with the net cofactor oxidation state being $(Mn^{IV})_4$ (**Figure 4*b***). The reason for the lack of a large XANES shift is that, due to the Mn ion being oxidized, it is also changing its ligand field (five to six coordinate) owing to the binding of an additional water molecule, as earlier suggested by Dau et al. (81). The recent X-ray studies and SFX data described above support this model (61, 66, 70). Computational models based on high-field EPR and electron–electron double resonance–detected NMR (EDNMR) data support O6 being a terminal OH to Mn1 (69, 82, 83). Most X-ray groups also favor O6 as a terminal OH (84, 85), although one group has suggested that it instead represents a terminal oxo ligand (86). In this latter instance, the deprotonated Mn^{IV}=O unit is modeled as having significant Mn^{III}–$O^\bullet$ character, as suggested in the very recent SFX structure by Suga et al. (71), inconsistent with the high-field EPR data described above.

EDNMR: electron–electron double resonance–detected NMR; technique to resolve hyperfine interactions

The last oxidation event has also been studied using time-resolved X-ray fluorescence measurements (87) (**Figure 4*c***). The evolution of this transition is described in terms of three discrete phases. A fast phase describing the oxidation of Y_Z is followed by a lag phase, in which no oxidation of the cofactor is observed. This lag phase is assigned based on kinetic isotope (H/D exchange) data to a deprotonation of the cofactor or of a neighboring amino-acid residue. In the final slow phase, the oxidized $Y_Z^{\bullet}$ is lost with the concomitant reformation of the S_0 state (indicated in **Figure 4*c***). These results suggest either that there is no metal-centered oxidation in the S_3 to S_0 transition, and that instead a ligand oxidation (oxyl-type intermediate) is likely formed, or that the mechanism involves a very short-lived Mn^V intermediate. Importantly, they exclude a long-lived peroxo-type intermediate, suggesting that the O–O bond formation step is rate limiting in this final phase. Subsequent measurements showing the absence of a slowing of the rate of O_2 formation at elevated O_2 pressures support this notion (88, 89). We note that a recent study by Pushkar et al. (90) has suggested that oxyl formation may occur during the lag phase, i.e., prior to $Y_Z^{\bullet}$ reduction. While consistent with the absence of a Mn-centered oxidation during the S_3 to S_0 transition, these results do imply transient formation of a Mn^{III}-oxyl inconsistent with the data in Reference 87.

As described in Section 2, it is important to recognize that oxidation of the cofactor is coupled to proton release. In this way, the redox potential of the cofactor remains approximately the same for all S state transitions. In the early S state transitions, deprotonation follows oxidation, while in the later S state transitions, as outlined above, it is instead the deprotonation event that occurs first (25) (see **Figure 6**). The S_1 to S_2 transition represents the switching point in which only electron transfer occurs (**Figure 1*d***). The (alternating) electron and proton release leads to an extended catalytic cycle for the water oxidation reaction in PS II, with nine states that differ in their net electron and proton count, which is indicated in **Figure 1*d*** (25, 26, 54). Pathways for proton egress have been examined through mutagenesis. In particular, two pathways have been identified with protons exiting via a channel that includes the Cl^- ion (**Figure 1*c***), which begins with the Asp61 residue (91–93), and a channel involving the Ca/Yz/His190. The way in which proton release is triggered by Y_Z oxidation is important. It has been suggested that a reordering of the solvating waters in the vicinity of the Y_Z can act to direct proton release, at least by the Asp61 channel (94), although other possibilities are being discussed (95, 96).

While a direct experimental determination of the protonation state of the cluster is not possible (owing to the large number of protons in the vicinity of the OEC), the protonation states of the ligated water molecules (W1–W4) can be inferred from magnetic resonance results together with density functional theory. Here, Ames et al. (50) performed calculations on a complete set of protonation configurations for the S_2 state of the OEC, based on the Umena et al. (46) structure, and compared these results with spectroscopic data (EPR/ENDOR and EXAFS). It was shown that the best agreement was obtained when all five oxygen bridges were deprotonated and one of the four bound water molecules at Mn4 (W2) was deprotonated, forming a hydroxo ligand, OH^-. Based on this key result, the protonation states of all S states can be inferred.

4.2. Cofactor Flexibility and Spin State Evolution

While SFX captures the key change in the stoichiometry of the cofactor during the S_2 to S_3 transition ($Mn_4CaO_5 \rightarrow Mn_4CaO_6$), it likely lacks the resolution at this point to characterize the dynamics of the cofactor. There is substantial evidence from many spectroscopic techniques that the cofactor can access more than one conformation, particularly in the S_2 state. Pantazis et al. (97) first proposed that the S_2 state of the OEC could exist in a closed cubane and an open cubane form, in which O5 occupies different positions (see **Figure 5*a***). The open cubane is referred to as the A form, while the closed cubane is the B form. The two structures have almost the same energy,

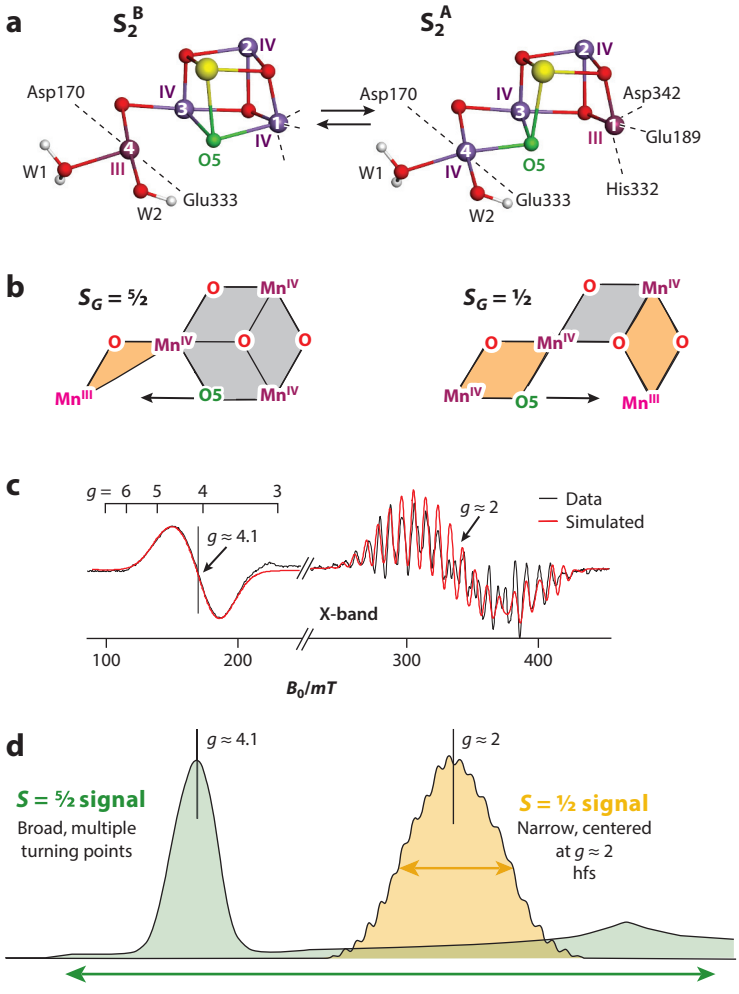

Figure 5

Valence isomers in the S_2 state of the OEC. (*a*) Geometries of the Mn_4CaO_5 cores showing a closed (*left*) and an open (*right*) cubane structure. (*b*) Spin exchange pathways with antiferromagnetic (*orange*) and ferromagnetic (*gray*) coupling resulting in different ground spin states, S_G (82, 83, 97). Note that the active oxygen (O5) is colored green. (*c*,*d*) Experimental (*c*) and simulated (*d*) X-band electron paramagnetic resonance spectra characterizing the two isomers (76, 83, 154, 155).

but the distribution of manganese oxidation states is different (97). This has been corroborated by other groups (98, 99).

An important consequence of this structural variation is that the cofactor in the S_2 state can access two different ground spin states. In the open cubane structure, the interactions between adjacent Mn ions are predominately antiferromagnetic, leading to a ground spin state that minimizes the number of effective unpaired electrons. In contrast, in the closed cubane structure, the interactions between adjacent Mn ions are predominately ferromagnetic, leading to a ground spin state that instead has a greater number of effective unpaired electrons (**Figure 5*b***). It is for this reason the two structures give rise to very different EPR signals: the low-spin ($S_G = 1/2$) multiline signal at $g \approx 2$ and the high-spin ($S_G = 5/2$) signal at $g \geq 4.1$ (see **Figure 5*c*,*d***). The S_2 state is

***S*, S_G:** electron spin, electron spin ground state

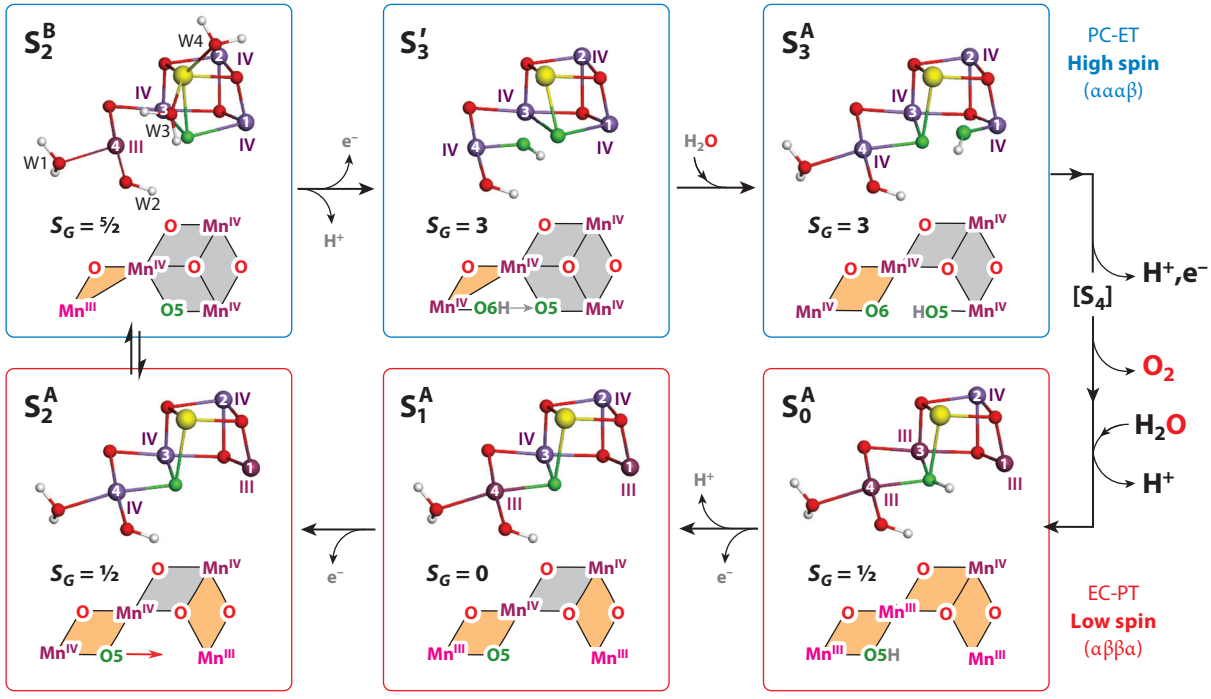

Figure 6

Structural, oxidation, and spin state evolution of the oxygen-evolving complex during the S state cycle (S_0 to S_3). In the early S states (S_0, S_1, and S_2^A), the cofactor adopts an open cubane structure, which exhibits a low-spin ground state. S state advancement follows electron then proton transfers (EC-PT). In the later S states (S_2^B, S_3', S_3), the cofactor always has an oxygen (*green*) inserted into the cubane unit. This changes the coupling and the ground spin state to high spin. S state advancement in this phase of the cycle follows proton then electron transfer (PC-ET) (54, 83). Note that only for state S_2^B are all four waters (W1–W4) shown; W3 and W4 are omitted for clarity in the other states.

unique in that it can display both of these spin state forms. In all S states preceding the S_2 state, the cofactor only adopts the lowest ground spin state (S_0, S_1), whereas in S states following the S_2 state, the cofactor only adopts higher ground spin states (S_3) (see **Figure 6**). The two spin state topologies have been correlated with resting and activated forms of the cofactor, and the high-spin state adopted in the S_3 state onwards is a requirement of the radical coupling mechanism described in Section 5 (54, 69, 83).

Recent XANES measurements (100) further support the above model for the two EPR signatures, with the two forms having a slightly different edge position. This is consistent with a redox isomerism, as the two Mn sites have different interactions with the protein, with the charge formed on Mn4 potentially being compensated by facile proton transfer to Asp61 (100) (**Figure 1*c***). EXAFS measurements also show that the two S_2 forms are structurally distinct. The data, however, do not allow an easy interpretation—they resolve a change in the ratio of Mn–Mn vector distances (100). Such structural changes are, however, highly unlikely at the low temperatures (<150 K) used to photoconvert the two forms (101). We note that the two S_2 state models described above should have similar Mn–Mn distances (one lengthens by ≈0.25 Å) but will differ in terms of the Mn–O bonds/distances, which could lead to the observed intensity changes (multiple scattering effects, etc.). The pH dependence of the two forms of the S_2 state also lends support to this model, explaining why the high-spin form is stabilized at elevated pH (102).

MIMS: membrane inlet mass spectrometry

A similar heterogeneity also likely exists in other S states. It is generally thought that S_0 and S_1 only occur in the open cubane (low-spin) conformation (82). However, the exact structure of the cofactor in both these states is dependent on the orientation of the Jahn–Teller axis for each of the Mn^{III} ions of the structure (82). Interconversion between these forms represents a more subtle change to the overall geometric and electronic structure, i.e., all forms of S_0 and S_1 adopt the same low-spin state (103, 104), but the spacing of the magnetic states is altered. In the higher S states (S_3), heterogeneity is instead correlated with the stepwise process of water molecule insertion, which is discussed in the next section.

4.3. Identification of the Two Substrate Molecules

The various crystal structures identify at least seven possible candidates for the two substrate waters, including the terminal water ligands of Mn4 and the Ca ion (W1–W4), the oxygen (μ-oxo) bridges of O4 and O5, and the new water-derived ligand to Mn1, O6. To further refine this picture, substrate-labeling experiments (^2H, $^{17,18}O$) have been performed, which allow many of these candidates to be excluded.

Primary information on the two substrate waters came from membrane inlet mass spectrometry (MIMS) (68, 105–108). In these experiments (**Figure 7*a,b***), labeled water ($H_2{}^{18}O$) was injected into the system and its incorporation into the product O_2 molecule subsequently measured. This measurement has been performed in all S states. The rate of exchange of bound substrate waters can be determined by varying the time in which the sample is incubated in labeled water (**Figure 7*b***). These experiments demonstrate that in all S states, both substrates exchange with bulk solvent, excluding early O–O bond formation, i.e., O–O bond/peroxide formation in the S_2 or S_3 state. They also show that the two substrates exchange at different rates [water slow (W_s) and water fast (W_f)], requiring the two bound substrates to be chemically distinct. The rates measured are in the range seen for terminal oxygen ligands of Mn ions in model systems and would seem to preclude Ca-bound waters, as these would exchange very rapidly ($1 \times 10^8\ s^{-1}$) (106, 107), or μ-oxo bridges, which instead exchange very slowly ($0.01\ s^{-1}$) (109, 110).

To further constrain this assignment, the same experiment was performed using magnetic resonance spectroscopy (111–114). In this experiment, $H_2{}^{17}O$-labeled water was used. Importantly, different bound oxygens (^{17}O sites) can be viewed separately, as they have a different spectroscopic signature in the ^{17}O EDNMR measurements (**Figure 7*c,d***). These experiments demonstrate that W1–W4 and, surprisingly, the oxygen bridge O5 exchange rapidly with bulk water (111–113). Recently, it was shown that the rate of O5 exchange approximately matches that of the slowly exchanging water ($\approx 1\ s^{-1}$), constraining this as one of the substrates of the reaction (L. Rapatskiy, personal communication). The relatively rapid rate of exchange of O5 is thought to be due to conformational flexibility (7, 108). More recently, it was shown that O5 represents a hydroxo in the S_0 state (115), explaining the enhanced exchange rate of the W_s in the S_0 state. The second (fast) substrate water, W_f, cannot yet be determined, owing to the time resolution of the measurements.

4.4. Pathways for Water Molecule Insertion

Crystallography does not yet completely resolve the sequence of events that lead to water molecule insertion during the S_2 to S_3 transition. As described above for the S_3 to S_0 transition (**Figure 4*c***), several distinct phases have been proposed (25, 116). Photoacoustic (116) and photothermal (25) experiments suggest four phases in the S_2–S_3 transition: (*a*) Yz oxidation within about 50 ns, (*b*) nuclear rearrangement within about 500 ns, (*c*) deprotonation in the immediate cofactor environment within about 50 μs, and (*d*) Mn oxidation by electron transfer from the cofactor to the

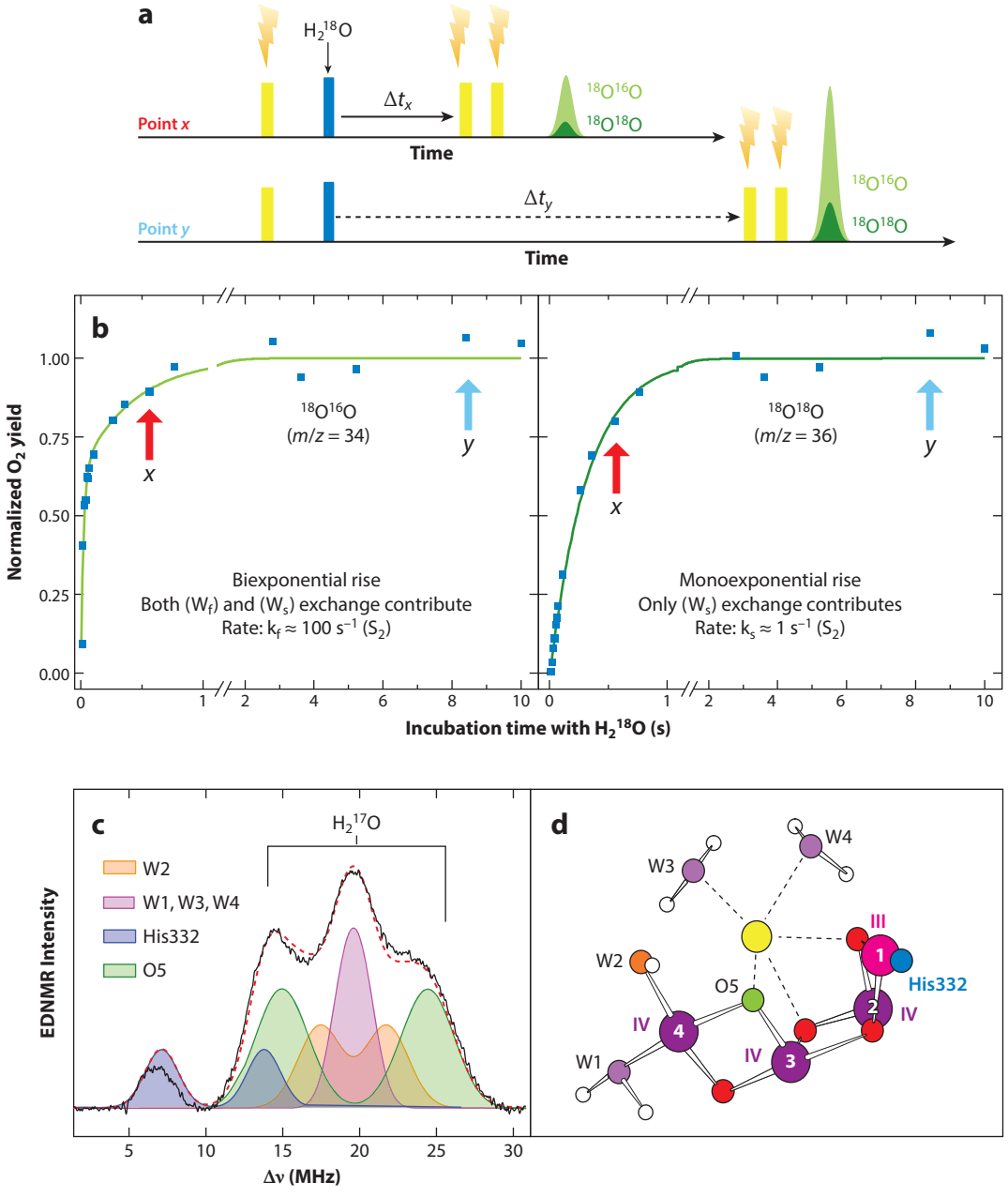

Figure 7

(*a*) Schematic of the membrane inlet mass spectrometry (MIMS) water exchange experiment (68, 105–107). After poising the cofactor in the S state of interest using short light flashes, labeled water ($H_2{}^{18}O$) is injected into the sample space. Another series of short light flashes leads to the release of labeled product O_2. By varying the incubation time Δt, the amount of labeled product changes, allowing the rate of exchange of bound substrate to be determined. (*b*) Water exchange curves measured for the two substrate sites, water fast (W_f) and water slow (W_s) (112, 156). Panel *b* adapted from Reference 112. (*c*) Corresponding spectroscopic data from ^{17}O electron–electron double resonance–detected NMR (EDNMR) showing the exchangeable substrate water sites (111–113). The exchange rate of O5 matches that seen for W_s in MIMS (L. Rapatskiy, personal communication). Panel *c* adapted from Reference 111. (*d*) Structure of the OEC (Mn_4CaO_5 cluster) with O5 indicated in green; see the color code in panel *c*.

oxidized Yz, directly coupled to proton transfer (within about 350 μs) (25). Mid-infrared measurements instead assign the third phase to a water network rearrangement in the vicinity of Yz and the fourth phase to both deprotonation and electron transfer (117). These results are potentially consistent with recent SFX data that demonstrate a lengthening of the Mn3–Mn4 vector that occurs during the fast (50 μs) phase, with incorporation of the new water-derived ligand (O6) instead occurring during the slow (350 μs) phase (70).

There have been many suggestions for how water insertion occurs. In the original model of Siegbahn (118, 119), the newly formed OH group on Mn1 is provided by a second-sphere water, or equally by one of the waters bound to the Ca (W3) (99, 120), which binds concertedly with its deprotonation in the $S_2 \rightarrow S_3$ step. In support of this mechanism, SFX data do resolve a small change in the position of Glu189, which is insufficient to allow direct water binding but is perhaps indicative of a larger conformational change allowing water access to Mn1 (70). This model, however, does not appear consistent with the kinetics of substrate exchange, as it would require a dramatic change in the exchange constant for the outer-sphere water that becomes a hydroxy ligand, in stark contrast to experimental data (105, 106). Furthermore, it has been shown in subsequent studies that this pathway for water delivery is not favorable energetically (121, 122).

Therefore, alternative pathways have been formulated that lead to the same type of final S_3 structure but in which the origin of substrates and the sequence of events in the $S_2 \rightarrow S_3$ transition are different (121, 122). These models are based on the cofactor's flexibility in the S_2 state. The basic idea is that conversion of the cofactor from an A-type, open cubane structure to a B-type, closed cubane structure more readily allows water binding. This is because the open coordination site of the cofactor is now located at the solvent-accessible Mn4, the terminus of two water channels to the cofactor, instead of at the solvent-inaccessible Mn1. Recent EPR measurements support this model, showing that the EPR signature of the closed cubane (B) form of the cofactor can advance to the S_3 state at low temperatures (250 K) while the open cubane (A) form cannot (123). High-field EPR data provide further support in identifying a modified S_3 intermediate (S_3'), in which cofactor oxidation has occurred but not water binding (124) (**Figure 4*b***). This new intermediate resembles a B-type closed cubane structure, in which the Mn4 is five coordinate (124) (see **Figure 5**).

Precisely which water then binds to Mn4 is an open question. One alternative described by Retegan et al. (121) is that water binds externally to the cluster on Mn4 via a channel associated with delivery of the substrate analog methanol (125–127). The final S_3 state is subsequently obtained by rotation of the Mn4 ligands and proton rearrangement. The substrates in this case can be identified as W2 and O5, both already present as ligands from the beginning of the cycle. This scenario better fits MIMS data that show both substrates to be already bound in the S_2 state (108).

An alternative proposal is that a Ca-bound water (W3) (99, 120, 128, 129) acts as the second substrate and is the water that forms the terminal OH ligand to a Mn ion in the $S_2 \rightarrow S_3$ transition to Mn4. This scenario similarly satisfies the requirement for both substrates to be bound in the S_2 state, although it is unclear how W3 (a water ligand to Ca) could have such a slow exchange rate, as described above. Note that for all mechanisms in which the newly inserted water binds to Mn, the labels of the oxygens O6 and O5 would need to be inverted as in **Figure 6**.

5. MECHANISMS FOR WATER OXIDATION IN PHOTOSYSTEM II

The recent SFX structures together with the spectroscopic and theoretical data described above limit possible O–O bond formation pathways in terms of both where the reaction occurs and how it occurs. If we first consider where the O–O bond formation step occurs, there are only two options: an O–O bond reaction that occurs either inside the cubane unit (internal reaction site, Mn1)

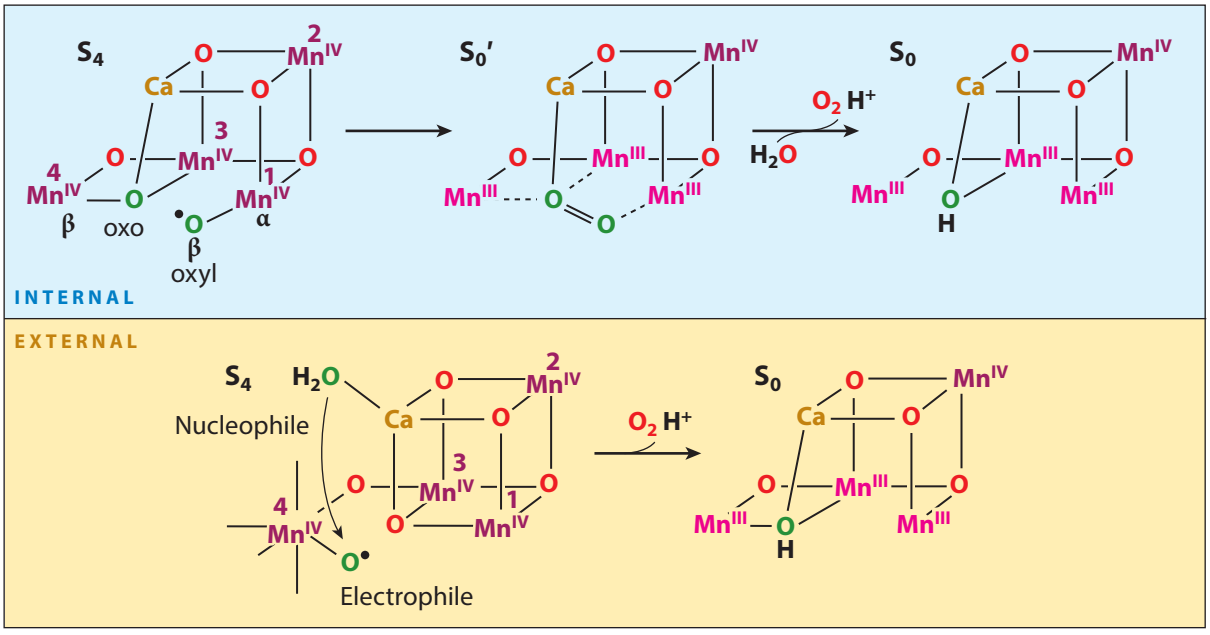

Figure 8

Representative O–O bond formation steps proposed for the oxygen-evolving complex. The two oxygens derived from the substrate waters are colored in green. In the top mechanism, O–O bond formation occurs internally, inside the cubane cage. This mechanism proceeds via an oxo-oxyl coupling, as originally proposed by Siegbahn (118, 135) and recently supported by Suga et al. (71). In this mechanism, the three Mn ions that bind the two substrates (product O_2) are reduced back to the +III level upon O–O bond formation, with the release of O_2 coupled to binding of the first substrate (O5) as a hydroxy ligand from water (115). In the bottom mechanism, the O–O bond formation instead occurs externally at the dangler (Mn4) ion. A Ca-bound nucleophile (W3) attacks the electrophilic O5 bound to Mn4 (134). For both pathways, alternate coupling mechanisms have been proposed that are described in the text. Note that in case of an external coupling, the second substrate could also be a terminal water ligand of the dangling Mn4.

or outside the cubane unit (external reaction site, Mn4). In both cases, one of the substrates is the oxygen ligand O5—see Section 4.3. Representative pathways for both of these two reaction sites are shown in **Figure 8**. The top mechanism represents a radical coupling and the bottom mechanism a nucleophilic attack, but alternative reaction sequences can be drawn (see discussion below). Both profiles provide a rationale for O6 insertion during the S_2 to S_3 transition. For internal reaction site pathways, O5 and O6 represent the substrates of the reaction and as such are required for O–O bond formation. For the external reaction site pathways, O6 may represent a substrate not of the current reaction cycle but of the next one, replacing the lost O5. This early reloading of the catalyst would have the advantage of lowering the barrier associated with reformation of the S_0 state.

This question can potentially be resolved in one of two ways. If the O–O bond formation step occurs inside the cubane unit, it may be possible to trap a structural intermediate using SFX during the $S_3 \rightarrow S_0$ transition in which the cubane unit is empty; i.e., after the release of product O_2, O5 and O6 would be absent, leaving an empty cavity. This, however, may be challenging, as theoretical modeling suggests water insertion and O_2 formation or release are likely concerted processes (130, 131). Alternatively, improved time resolution of the combined mass spectrometry/spectroscopy measurements described in Section 4.3, targeting the bound substrates in the S_3 state, could also address this question.

It is more difficult to experimentally demonstrate how the two oxygens join together. There are two archetypal mechanisms described in the literature, which we briefly describe below: (*a*) an acid–base coupling, i.e., the nucleophilic attack of a water or hydroxo group to an electrophilic terminal oxo (either Mn^{IV}-oxyl or Mn^{V}-oxo); or (*b*) radical-type coupling between two oxyl or oxo/oxyl groups (15, 98, 118, 132–134). We note that while these two mechanisms are described as distinctly different, the reaction could have an admixture of both characters. It should also be stressed that the O–O bond formation event is only one part of the S_3 to S_0 transition, which also involves proton release, electron transfer, and product release coupled to the uptake of a new substrate, which has been modeled extensively (15, 130, 131, 135–139) but is not covered in depth here.

The nucleophilic attack or acid/base-type reaction mechanism is the experimentally observed mechanism in simpler chemical models using first-row transition metals (see, e.g., 140). In such a mechanism, an electron-deficient oxygen (electrophile) of a high-valent Mn ion is open to the chemical attack of a nearby water nucleophile (133, 134). Initially it was envisaged that the electrophile would represent a Mn^{V}-oxo, although it is now thought that a Mn^{IV}-oxyl could also fulfill this role. While attractive in its simplicity, comparatively large barriers have been estimated for this mechanism (141).

The radical coupling mechanism has instead only been definitely demonstrated in simpler (monomeric, dimeric) second-row transition metal catalysts (Ru, Ir), which can more easily access two-electron chemistry (142, 143). The first proposal of a radical coupling between two caged oxygens was that of Siegbahn (118, 119). His mechanism invoked the formation of a terminal Mn^{IV}-oxyl (O6), which then reacted with the nearby O5, forming the O–O bond (119, 135). This type of mechanism has been described as oxo/oxyl coupling (119, 135, 139). In principle, the oxyl could instead be O5, which would then attack O6.

There are, however, alternative ideas about how such a coupling could occur. An interesting recent proposal by Shoji et al. (137) and Pushkar et al. (90) stated that the O–O bond can form while already in the presence of the tyrosyl radical (i.e., nominally in the $S_3Y_Z^{\bullet}$ state) coupled with intramolecular proton transfer. This pathway avoids a formal S_4 intermediate, because O–O bond formation is initiated—and hence one of the four Mn^{IV} ions is reduced to Mn^{III}—before the tyrosyl radical of the $S_3Y_Z^{\bullet}$ intermediate is reduced. The observation that substrate exchange is arrested in the lag phase may be consistent with such a mechanism (144), although at the same time, reduction of a Mn^{IV} ion to Mn^{III} is not observed (87). Similar ideas have been invoked by the groups of Yamaguchi (145) and O'Malley (146), who have speculated that O–O bond formation may occur in the S_3 state. Early-onset O–O bond formation mechanisms have been discussed for many years (147) but in recent times have been excluded on the basis of spectroscopic data (water exchange measurements; see Section 4.3). Such a mechanism thus requires that the peroxo species formed in the S_3 state represents a small minority species, which is preferentially oxidized by the tyrosyl radical. Other radical coupling mechanisms assume different assignments of the two substrates, i.e., a coupling of two ligands of the Mn4, O5, and W2 proposed by Zhang & Sun (148). Again, these types of mechanisms do not seem to be immediately consistent with spectroscopic data, invoking a Mn^{VII} intermediate (see Section 4.1). For a more detailed description of these mechanisms, see Pantazis (15, 67).

6. CONCLUSIONS, REMAINING PROBLEMS, AND FUTURE CHALLENGES

Since the development of the first model for the catalytic cycle (23), our understanding of biological water oxidation has made enormous progress. Advances in crystallography and spectroscopy

from the last 10 years are now poised to answer one of nature's big questions: how to split water. There is now consensus about the structure of the catalyst in its resting state and that a water molecule is inserted into the cubane unit during the catalyst's final metastable transition, S_2 to S_3, although its origin is debated. Similarly, the oxidation and spin states of all metastable intermediates (S_0, S_1, S_2, and S_3) and the identification of at least one of the substrates of the reaction (O5) have been resolved. What remains is a complete description of the O–O bond formation step (S_4), its release from the cofactor, and the reformation of the catalyst coupled to water insertion.

Clearly, further experimental data targeting these final steps of catalysis are needed. Better SFX structures appear to have already excluded the early-onset O–O bond formation mechanisms described above, in line with earlier spectroscopic results. What is needed is to continue this structural feat toward resolution of the cofactor in the lag-phase and subsequent O_2 release and water-binding events of the S_3 to S_0 transition. While these phases are short, they can be slowed up to 100-fold in chemically modified systems (149–151). Such modifications include (*a*) replacing the Ca^{2+} with Sr^{2+} and the second sphere Cl^- ion with Br^- or I^- and (*b*) mutation of residues in the vicinity of O5 such as Val185, which sits directly in front of this oxygen and prevents water access to this face of the cofactor, and Asp61, which instead hydrogen bonds to the W1 ligand of Mn4 and participates in proton egress. Such modified systems may allow detection of intermediates, including a bound superoxo or peroxo adduct, the unloaded or empty catalyst following the loss of the O_2 product, and locate where and when water binds. Coupled with spectroscopy and high-level theory, such changes could be correlated with the series of electron and proton transfer steps, including the trapping of an oxyl-type intermediate.

DISCLOSURE STATEMENT

The authors are not aware of any affiliations, memberships, funding, or financial holdings that might be perceived as affecting the objectivity of this review.

ACKNOWLEDGMENTS

This work has been supported by the Max Planck Society and the Australian Research Council (FT140100834). We thank Professors Richard Debus (University of California, Riverside) and Holger Dau (Freie Universität Berlin) for their help in revising the text.

LITERATURE CITED

1. Fischer WW, Hemp J, Johnson JE. 2016. Evolution of oxygenic photosynthesis. *Annu. Rev. Earth Planet. Sci.* 44:647–83
2. Hamilton TL, Bryant DA, Macalady JL. 2016. The role of biology in planetary evolution: cyanobacterial primary production in low-oxygen Proterozoic oceans. *Environ. Microbiol.* 18:325–40
3. acatech, Nat. Acad. Sci. Eng., Ger. Nat. Acad. Sci. Leopoldina, Union Ger. Acad. Sci. Hum., eds. 2018. *Artificial photosynthesis: state of research, scientific-technological challenges and perspectives*. Position Pap., acatech, Nat. Acad. Sci. Eng., Ger. Nat. Acad. Sci. Leopoldina, Union Ger. Acad. Sci. Hum., Munich
4. Chabi S, Papadantonakis KM, Lewis NS, Freund MS. 2017. Membranes for artificial photosynthesis. *Energy Environ. Sci.* 10:1320–38
5. Collings AF, Critchley C, eds. 2005. *Artificial Photosynthesis: From Basic Biology to Industrial Application*. Chichester, UK: Wiley
6. Cox N, Lubitz W. 2013. Molecular concepts of water splitting: nature's approach. In *Chemical Energy Storage*, ed. R Schlögl, pp. 185–224. Berlin: De Gruyter GmbH
7. Cox N, Pantazis DA, Neese F, Lubitz W. 2015. Artificial photosynthesis: understanding water splitting in nature. *Interface Focus* 5:20150009

8. Faunce TA, Lubitz W, Rutherford AW, MacFarlane DR, Moore GF, et al. 2013. Energy and environment policy case for a global project on artificial photosynthesis. *Energy Environ. Sci.* 6:695–98
9. Gratzel M. 2005. Solar energy conversion by dye-sensitized photovoltaic cells. *Inorg. Chem.* 44:6841–51
10. McKone JR, Crans DC, Martin C, Turner J, Duggal AR, Gray HB. 2016. Translational science for energy and beyond. *Inorg. Chem.* 55:9131–43
11. Nocera DG. 2012. The artificial leaf. *Acc. Chem. Res.* 45:767–76
12. Nocera DG. 2017. Solar fuels and solar chemicals industry. *Acc. Chem. Res.* 50:616–19
13. Messinger J, Lubitz W, Shen JR, eds. 2014. Photosynthesis: from natural to artificial. Special issue, *Phys. Chem. Chem. Phys.* 16
14. Junge W. 2019. Oxygenic photosynthesis: history, status and perspective. *Q. Rev. Biophys.* 52:e1, 1–17
15. Pantazis DA. 2018. Missing pieces in the puzzle of biological water oxidation. *ACS Catal.* 8:9477–507
16. Shen J-R. 2015. The structure of photosystem II and the mechanism of water oxidation in photosynthesis. *Annu. Rev. Plant Biol.* 66:23–48
17. Vinyard DJ, Brudvig GW. 2017. Progress toward a molecular mechanism of water oxidation in photosystem II. *Annu. Rev. Phys. Chem.* 68:101–16
18. Yano J, Yachandra V. 2014. Mn_4Ca cluster in photosynthesis: where and how water is oxidized to dioxygen. *Chem. Rev.* 114:4175–205
19. Barber J. 2017. A mechanism for water splitting and oxygen production in photosynthesis. *Nat. Plants* 3:17041
20. Lubitz W, Chrysina M, Cox N. 2019. Water oxidation in photosystem II. *Photosynth. Res.* 142:105–25
21. Wydrzynski T, Satoh K, eds. 2005. *Photosystem II, The Light-Driven Water: Plastoquinone Oxidoreductase*. Netherlands: Springer
22. Joliot P, Barbieri G, Chabaud R. 1969. A new model of photochemical centers in system 2. *Photochem. Photobiol.* 10:309–29
23. Kok B, Forbush B, McGloin M. 1970. Cooperation of charges in photosynthetic O_2 evolution—1. A linear four step mechanism. *Photochem. Photobiol.* 11:457–75
24. Nilsson H, Cournac L, Rappaport F, Messinger J, Lavergne J. 2016. Estimation of the driving force for dioxygen formation in photosynthesis. *Biochim. Biophys. Acta* 1857:23–33
25. Klauss A, Haumann M, Dau H. 2012. Alternating electron and proton transfer steps in photosynthetic water oxidation. *PNAS* 109:16035–40
26. Klauss A, Haumann M, Dau H. 2015. Seven steps of alternating electron and proton transfer in photosystem II water oxidation traced by time-resolved photothermal beam deflection at improved sensitivity. *J. Phys. Chem. B* 119:2677–89
27. Suzuki H, Sugiura M, Noguchi T. 2009. Monitoring proton release during photosynthetic water oxidation in photosystem II by means of isotope-edited infrared spectroscopy. *J. Am. Chem. Soc.* 131:7849–57
28. Dau H, Haumann M. 2007. Eight steps preceding O-O bond formation in oxygenic photo synthesis—a basic reaction cycle of the photosystem II manganese complex. *Biochim. Biophys. Acta* 1767:472–83
29. Schlodder E, Witt HT. 1999. Stoichiometry of proton release from the catalytic center in photosynthetic water oxidation—reexamination by a glass electrode study at pH 5.5–7.2. *J. Biol. Chem.* 274:30387–92
30. Nixon PJ, Michoux F, Yu JF, Boehm M, Komenda J. 2010. Recent advances in understanding the assembly and repair of photosystem II. *Ann. Bot.* 106:1–16
31. Järvi S, Suorsa M, Aro E-M. 2015. Photosystem II repair in plant chloroplasts—regulation, assisting proteins and shared components with photosystem II biogenesis. *Biochim. Biophys. Acta Bioenerget.* 1847:900–9
32. Vass I, Aro E-M. 2008. Photoinhibition of photosynthetic electron transport. In *Primary Processes of Photosynthesis*, Part 1*: Basic Principles and Apparatus*, ed. G Renger, pp. 393–425. Cambridge: Royal Soc. Chem.
33. van Wijk KJ, Nilsson LO, Styring S. 1994. Synthesis of reaction center proteins and reactivation of redox components during repair of photosystem II after light-induced inactivation. *J. Biol. Chem.* 269:28382–92
34. Messinger J, Renger G. 2008. Photosynthetic water splitting. In *Primary Processes of Photosynthesis*, Part 2*: Principles and Apparatus*, ed. G Renger, pp. 291–349. Cambridge: Royal Soc. Chem.

35. Krieger-Liszkay A, Fufezan C, Trebst A. 2008. Singlet oxygen production in photosystem II and related protection mechanism. *Photosynth. Res.* 98:551–64
36. Deisenhofer J, Epp O, Miki K, Huber R, Michel H. 1985. Structure of the protein subunits in the photosynthetic reaction center of *Rhodopseudomonas viridis* at 3 Å resolution. *Nature* 318:618–24
37. Jordan P, Fromme P, Witt HT, Klukas O, Saenger W, Krauß N. 2001. Three-dimensional structure of cyanobacterial photosystem I at 2.5 Å resolution. *Nature* 411:909–17
38. Zouni A, Witt HT, Kern J, Fromme P, Krauss N, et al. 2001. Crystal structure of photosystem II from *Synechococcus elongatus* at 3.8 Å resolution. *Nature* 409:739–43
39. Hoganson CW, Babcock GT. 1997. A metalloradical mechanism for the generation of oxygen from water in photosynthesis. *Science* 277:1953–56
40. Yano J, Kern J, Irrgang KD, Latimer MJ, Bergmann U, et al. 2005. X-ray damage to the Mn_4Ca complex in single crystals of photosystem II: a case study for metalloprotein crystallography. *PNAS* 102:12047–52
41. Grabolle M, Haumann M, Müller C, Liebisch P, Dau H. 2006. Rapid loss of structural motifs in the manganese complex of oxygenic photosynthesis by X-ray irradiation at 10–300 K. *J. Biol. Chem.* 281:4580–88
42. Ferreira KN, Iverson TM, Maghlaoui K, Barber J, Iwata S. 2004. Architecture of the photosynthetic oxygen-evolving center. *Science* 303:1831–38
43. Robblee JH, Cinco RM, Yachandra VK. 2001. X-ray spectroscopy-based structure of the Mn cluster and mechanism of photosynthetic oxygen evolution. *Biochim. Biophys. Acta Bioenerget.* 1503:7–23
44. Peloquin JM, Campbell KA, Randall DW, Evanchik MA, Pecoraro VL, et al. 2000. ^{55}Mn ENDOR of the S_2 state multiline EPR signal of photosystem II: implications on the structure of the tetranuclear Mn cluster. *J. Am. Chem. Soc.* 122:10926–42
45. Peloquin JM, Britt RD. 2001. EPR/ENDOR characterization of the physical and electronic structure of the OEC Mn cluster. *Biochim. Biophys. Acta Bioenerget.* 1503:96–111
46. Umena Y, Kawakami K, Shen J-R, Kamiya N. 2011. Crystal structure of oxygen-evolving photosystem II at a resolution of 1.9 Å. *Nature* 473:55–60
47. Yano J, Pushkar Y, Glatzel P, Lewis A, Sauer K, et al. 2005. High-resolution Mn EXAFS of the oxygen-evolving complex in photosystem II: structural implications for the Mn_4Ca cluster. *J. Am. Chem. Soc.* 127:14974–75
48. Dau H, Grundmeier A, Loja P, Haumann M. 2008. On the structure of the manganese complex of photosystem II: extended-range EXAFS data and specific atomic-resolution models for four S-states. *Philos. Trans. R. Soc. B* 363:1237–43
49. Luber S, Rivalta I, Umena Y, Kawakami K, Shen J-R, et al. 2011. S_1-state model of the O_2-evolving complex of photosystem II. *Biochemistry* 50:6308–11
50. Ames W, Pantazis DA, Krewald V, Cox N, Messinger J, et al. 2011. Theoretical evaluation of structural models of the S_2 state in the oxygen evolving complex of photosystem II: protonation states and magnetic interactions. *J. Am. Chem. Soc.* 133:19743–57
51. Galstyan A, Robertazzi A, Knapp EW. 2012. Oxygen-evolving Mn cluster in photosystem II: the protonation pattern and oxidation state in the high-resolution crystal structure. *J. Am. Chem. Soc.* 134:7442–49
52. Hirata K, Shinzawa-Itoh K, Yano N, Takemura S, Kato K, et al. 2014. Determination of damage-free crystal structure of an X-ray–sensitive protein using an XFEL. *Nat. Methods* 11:734–36
53. Suga M, Akita F, Hirata K, Ueno G, Murakami H, et al. 2015. Native structure of photosystem II at 1.95 Å resolution viewed by femtosecond X-ray pulses. *Nature* 517:99–103
54. Perez-Navarro M, Neese F, Lubitz W, Pantazis DA, Cox N. 2016. Recent developments in biological water oxidation. *Curr. Opin. Chem. Biol.* 31:113–19
55. Neutze R, Wouts R, van der Spoel D, Weckert E, Hajdu J. 2000. Potential for biomolecular imaging with femtosecond X-ray pulses. *Nature* 406:752–57
56. Chapman HN, Fromme P, Barty A, White TA, Kirian RA, et al. 2011. Femtosecond X-ray protein nanocrystallography. *Nature* 470:73–77
57. Johansson LC, Arnlund D, White TA, Katona G, DePonte DP, et al. 2012. Lipidic phase membrane protein serial femtosecond crystallography. *Nat. Methods* 9:263–65
58. Kern J, Alonso-Mori R, Tran R, Hattne J, Gildea RJ, et al. 2013. Simultaneous femtosecond X-ray spectroscopy and diffraction of photosystem II at room temperature. *Science* 340:491–95

59. Kern J, Hattne J, Tran R, Alonso-Mori R, Laksmono H, et al. 2014. Methods development for diffraction and spectroscopy studies of metalloenzymes at X-ray free-electron lasers. *Philos. Trans. R. Soc. B* 369:20130590
60. Kern J, Alonso-Mori R, Hellmich J, Tran R, Hattne J, et al. 2012. Room temperature femtosecond X-ray diffraction of photosystem II microcrystals. *PNAS* 109:9721–26
61. Kupitz C, Basu S, Grotjohann I, Fromme R, Zatsepin NA, et al. 2014. Serial time-resolved crystallography of photosystem II using a femtosecond X-ray laser. *Nature* 513:261–65
62. Askerka M, Wang J, Vinyard DJ, Brudvig GW, Batista VS. 2016. S_3 state of the O_2-evolving complex of photosystem II: insights from QM/MM, EXAFS, and femtosecond X-ray diffraction. *Biochemistry* 55:981–84
63. Kern J, Tran R, Alonso-Mori R, Koroidov S, Echols N, et al. 2014. Taking snapshots of photosynthetic water oxidation using femtosecond X-ray diffraction and spectroscopy. *Nat. Commun.* 5:4371
64. Young ID, Ibrahim M, Chatterjee R, Gul S, Fuller FD, et al. 2016. Structure of photosystem II and substrate binding at room temperature. *Nature* 540:453–57
65. Sauter NK, Echols N, Adams PD, Zwart PH, Kern J, et al. 2016. No observable conformational changes in PSII. *Nature* 533:E1–2
66. Suga M, Akita F, Sugahara M, Kubo M, Nakajima Y, et al. 2017. Light-induced structural changes and the site of O=O bond formation in PSII caught by XFEL. *Nature* 543:131–35
67. Pantazis DA. 2019. The S_3 state of the oxygen-evolving complex: overview of spectroscopy and XFEL crystallography with a critical evaluation of early-onset models for O–O bond formation. *Inorganics* 7:55
68. Messinger J, Badger M, Wydrzynski T. 1995. Detection of one slowly exchanging substrate water molecule in the S_3 state of photosystem II. *PNAS* 92:3209–13
69. Cox N, Retegan M, Neese F, Pantazis DA, Boussac A, Lubitz W. 2014. Electronic structure of the oxygen-evolving complex in photosystem II prior to O-O bond formation. *Science* 345:804–8
70. Kern J, Chatterjee R, Young ID, Fuller FD, Lassalle L, et al. 2018. Structures of the intermediates of Kok's photosynthetic water oxidation clock. *Nature* 563:421–25
71. Suga M, Akita F, Yamashita K, Nakajima Y, Ueno G, et al. 2019. An oxyl/oxo mechanism for oxygen-oxygen coupling in PSII revealed by an X-ray free-electron laser. *Science* 366:334–38
72. Mukherjee S, Stull JA, Yano J, Stamatatos TC, Pringouri K, et al. 2012. Synthetic model of the asymmetric [Mn_3CaO_4] cubane core of the oxygen-evolving complex of photosystem II. *PNAS* 109:2257–62
73. Kanady JS, Tsui EY, Day MW, Agapie T. 2011. A synthetic model of the Mn_3Ca subsite of the oxygen-evolving complex in photosystem II. *Science* 333:733–36
74. Spatzal T, Aksoyoglu M, Zhang L, Andrade SLA, Schleicher E, et al. 2011. Evidence for interstitial carbon in nitrogenase FeMo cofactor. *Science* 334:940
75. Tanaka A, Fukushima Y, Kamiya N. 2017. Two different structures of the oxygen-evolving complex in the same polypeptide frameworks of photosystem II. *J. Am. Chem. Soc.* 139:1718–21
76. Dismukes GC, Siderer Y. 1981. Intermediates of a polynuclear manganese center involved in photosynthetic oxidation of water. *PNAS* 78:274–78
77. Messinger J, Robblee JH, Bergmann U, Fernandez C, Glatzel P, et al. 2001. Absence of Mn-centered oxidation in the $S_2 \rightarrow S_3$ transition: implications for the mechanism of photosynthetic water oxidation. *J. Am. Chem. Soc.* 123:7804–20
78. Haumann M, Muller C, Liebisch P, Iuzzolino L, Dittmer J, et al. 2005. Structural and oxidation state changes of the photosystem II manganese complex in four transitions of the water oxidation cycle ($S_0 \rightarrow S_1$, $S_1 \rightarrow S_2$, $S_2 \rightarrow S_3$, and S_3,$S_4 \rightarrow S_0$) characterized by X-ray absorption spectroscopy at 20 K and room temperature. *Biochemistry* 44:1894–908
79. Kulik LV, Epel B, Lubitz W, Messinger J. 2005. ^{55}Mn pulse ENDOR at 34 GHz of the S_0 and S_2 states of the oxygen-evolving complex in photosystem II. *J. Am. Chem. Soc.* 127:2392–93
80. Kulik LV, Epel B, Lubitz W, Messinger J. 2007. Electronic structure of the Mn_4O_xCa cluster in the S_0 and S_2 states of the oxygen-evolving complex of photosystem II based on pulse ^{55}Mn-ENDOR and EPR spectroscopy. *J. Am. Chem. Soc.* 129:13421–35

81. Dau H, Liebisch P, Haumann M. 2005. The manganese complex of oxygenic photosynthesis conversion of five-coordinated Mn(III) to six-coordinated Mn(IV) in the S_2-S_3 transition is implied by XANES simulations. *Phys. Scr.* T115:844–46
82. Krewald V, Retegan M, Cox N, Messinger J, Lubitz W, et al. 2015. Metal oxidation states in biological water splitting. *Chem. Sci.* 6:1676–95
83. Krewald V, Retegan M, Neese F, Lubitz W, Pantazis DA, Cox N. 2016. Spin state as a marker for the structural evolution of nature's water splitting catalyst. *Inorg. Chem.* 55:488–501
84. Zaharieva I, Chernev P, Berggren G, Anderlund M, Styring S, et al. 2016. Room-temperature energy-sampling Kβ X-ray emission spectroscopy of the Mn_4Ca complex of photosynthesis reveals three manganese-centered oxidation steps and suggests a coordination change prior to O_2 formation. *Biochemistry* 55:4197–211
85. Zaharieva I, Dau H, Haumann M. 2016. Sequential and coupled proton and electron transfer events in the $S_2 \rightarrow S_3$ transition of photosynthetic water oxidation revealed by time-resolved X-ray absorption spectroscopy. *Biochemistry* 55:6996–7004
86. Davis KM, Pushkar YN. 2015. Structure of the oxygen evolving complex of photosystem II at room temperature. *J. Phys. Chem. B* 119:3492–98
87. Haumann M, Liebisch P, Müller C, Barra M, Grabolle M, Dau H. 2005. Photosynthetic O_2 formation tracked by time-resolved X-ray experiments. *Science* 310:1019–21
88. Haumann M, Grundmeier A, Zaharieva I, Dau H. 2008. Photosynthetic water oxidation at elevated dioxygen partial pressure monitored by time-resolved X-ray absorption measurements. *PNAS* 105:17384–89
89. Kolling DRJ, Brown TS, Ananyev G, Dismukes GC. 2009. Photosynthetic oxygen evolution is not reversed at high oxygen pressures: mechanistic consequences for the water-oxidizing complex. *Biochemistry* 48:1381–89
90. Pushkar Y, Davis KM, Palenik MC. 2018. Model of the oxygen evolving complex which is highly predisposed to O–O bond formation. *J. Phys. Chem. Lett.* 9:3525–31
91. Narzi D, Bovi D, Guidoni L. 2014. Pathway for Mn-cluster oxidation by tyrosine-Z in the S_2 state of photosystem II. *PNAS* 111:8723–28
92. Rivalta I, Amin M, Luber S, Vassiliev S, Pokhrel R, et al. 2011. Structural-functional role of chloride in photosystem II. *Biochemistry* 50:6312–15
93. Debus RJ. 2014. Evidence from FTIR difference spectroscopy that D1-Asp61 influences the water reactions of the oxygen-evolving Mn_4CaO_5 cluster of photosystem II. *Biochemistry* 53:2941–55
94. Retegan M, Cox N, Lubitz W, Neese F, Pantazis DA. 2014. The first tyrosyl radical intermediate formed in the S_2-S_3 transition of photosystem II. *Phys. Chem. Chem. Phys.* 16:11901–10
95. Takemoto H, Sugiura M, Noguchi T. 2019. Proton release process during the S_2-to-S_3 transition of photosynthetic water oxidation as revealed by the pH dependence of kinetics monitored by time-resolved infrared spectroscopy. *Biochemistry* 58:4276–83
96. Chrysina M, de Mendonça Silva JC, Zahariou G, Pantazis DA, Ionnidis N. 2019. Proton translocation via tautomerization of Asn298 during the S_2-S_3 state transition in the oxygen evolving complex of photosystem II. *J. Phys. Chem. B* 123:3068–78
97. Pantazis DA, Ames W, Cox N, Lubitz W, Neese F. 2012. Two interconvertible structures that explain the spectroscopic properties of the oxygen-evolving complex of photosystem II in the S_2 state. *Angew. Chem. Int. Ed.* 51:9935–40
98. Saito T, Yamanaka S, Kanda K, Isobe H, Takano Y, et al. 2012. Possible mechanisms of water splitting reaction based on proton and electron release pathways revealed for $CaMn_4O_5$ cluster of PSII refined to 1.9 Å X-ray resolution. *Int. J. Quantum Chem.* 112:253–76
99. Bovi D, Narzi D, Guidoni L. 2013. The S_2 state of the oxygen evolving complex of photosystem II explored by QM/MM dynamics: Spin surfaces and metastable states suggest a reaction path towards the S_3 state. *Angew. Chem. Int. Ed.* 52:11744–49
100. Chatterjee R, Lassalle L, Gul S, Fuller FD, Young ID, et al. 2019. Structural isomers of the S_2 state in photosystem II: Do they exist at room temperature and are they important for function? *Physiol. Plant.* 166:60–72

101. Boussac A, Girerd JJ, Rutherford AW. 1996. Conversion of the spin state of the manganese complex in photosystem II induced by near-infrared light. *Biochemistry* 35:6984–89
102. Boussac A, Ugur I, Marion A, Sugiura M, Kaila VRI, Rutherford AW. 2018. The low spin–high spin equilibrium in the S_2-state of the water oxidizing enzyme. *Biochim. Biophys. Acta* 1859:342–56
103. Ahrling KA, Peterson S, Styring S. 1997. An oscillating manganese electron paramagnetic resonance signal from the S_0 state of the oxygen evolving complex in photosystem II. *Biochemistry* 36:13148–52
104. Messinger J, Robblee JH, Yu WO, Sauer K, Yachandra VK, Klein MP. 1997. The S_0 state of the oxygen-evolving complex in photosystem II is paramagnetic: detection of EPR multiline signal. *J. Am. Chem. Soc.* 119:11349–50
105. Hillier W, Messinger J, Wydrzynski T. 1998. Kinetic determination of the fast exchanging substrate water molecule in the S_3 state of photosystem II. *Biochemistry* 37:16908–14
106. Hillier W, Wydrzynski T. 2000. The affinities for the two substrate water binding sites in the O_2 evolving complex of photosystem II vary independently during S-state turnover. *Biochemistry* 39:4399–405
107. Hillier W, Wydrzynski T. 2004. Substrate water interactions within the photosystem II oxygen evolving complex. *Phys. Chem. Chem. Phys.* 6:4882–89
108. Cox N, Messinger J. 2013. Reflections on substrate water and dioxygen formation. *Biochim. Biophys. Acta* 1827:1020–30
109. Tagore R, Chen HY, Crabtree RH, Brudvig GW. 2006. Determination of μ-oxo exchange rates in di-μ-oxo dimanganese complexes by electrospray ionization mass spectrometry. *J. Am. Chem. Soc.* 128:9457–65
110. McConnell IL, Grigoryants VM, Scholes CP, Myers WK, Chen P-Y, et al. 2012. EPR-ENDOR characterization of (^{17}O, ^{1}H, ^{2}H) water in manganese catalase and its relevance to the oxygen-evolving complex of photosystem II. *J. Am. Chem. Soc.* 134:1504–12
111. Rapatskiy L, Cox N, Savitsky A, Ames WM, Sander J, et al. 2012. Detection of the water-binding sites of the oxygen-evolving complex of photosystem II using W-band ^{17}O electron–electron double resonance-detected NMR spectroscopy. *J. Am. Chem. Soc.* 134:16619–34
112. Navarro MP, Ames WM, Nilsson H, Lohmiller T, Pantazis DA, et al. 2013. Ammonia binding to the oxygen-evolving complex of photosystem II identifies the solvent-exchangeable oxygen bridge (μ-oxo) of the manganese tetramer. *PNAS* 110:15561–66
113. Lohmiller T, Krewald V, Navarro MP, Retegan M, Rapatskiy L, et al. 2014. Structure, ligands and substrate coordination of the oxygen-evolving complex of photosystem II in the S_2 state: a combined EPR and DFT study. *Phys. Chem. Chem. Phys.* 16:11877–92
114. Rapatskiy L, Ames WM, Perez-Navarro M, Savitsky A, Griese JJ, et al. 2015. Characterization of oxygen bridged manganese model complexes using multifrequency ^{17}O-hyperfine EPR spectroscopies and density functional theory. *J. Phys. Chem. Lett. B* 119:13904–21
115. Lohmiller T, Krewald V, Sedoud A, Rutherford AW, Neese F, et al. 2017. The first state in the catalytic cycle of the water-oxidizing enzyme: identification of a water-derived μ-hydroxo bridge. *J. Am. Chem. Soc.* 139:14412–24
116. Klauss A, Sikora T, Suss B, Dau H. 2012. Fast structural changes (200–900 ns) may prepare the photosynthetic manganese complex for oxidation by the adjacent tyrosine radical. *Biochim. Biophys. Acta* 1817:1196–207
117. Sakamoto H, Shimizu T, Nagao R, Noguchi T. 2017. Monitoring the reaction process during the $S_2 \rightarrow S_3$ transition in photosynthetic water oxidation using time-resolved infrared spectroscopy. *J. Am. Chem. Soc.* 139:2022–29
118. Siegbahn PEM. 2009. Structures and energetics for O_2 formation in photosystem II. *Acc. Chem. Res.* 42:1871–80
119. Siegbahn PEM. 2012. Mechanisms for proton release during water oxidation in the S_2 to S_3 and S_3 to S_4 transitions in photosystem II. *Phys. Chem. Chem. Phys.* 14:4849–56
120. Ugur I, Rutherford AW, Kaila VRI. 2016. Redox-coupled substrate water reorganization in the active site of photosystem II—the role of calcium in substrate water delivery. *Biochim. Biophys. Acta* 1857:740–48

121. Retegan M, Krewald V, Mamedov F, Neese F, Lubitz W, et al. 2016. A five-coordinate Mn(IV) intermediate in biological water oxidation: spectroscopic signature and a pivot mechanism for water binding. *Chem. Sci.* 7:72–84
122. Capone M, Narzi D, Bovi D, Guidoni L. 2016. Mechanism of water delivery to the active site of photosystem II along the S_2 to S_3 transition. *J. Phys. Chem. Lett.* 7:592–96
123. Boussac A. 2019. Temperature dependence of the high-spin S_2 to S_3 transition in photosystem II: mechanistic consequences. *Biochim. Biophys. Acta Bioenerget.* 1860:508–18
124. Chrysina M, Heyno E, Kutin Y, Reus M, Nilsson H, et al. 2019. Five-coordinate Mn^{IV} intermediate in the activation of nature's water splitting cofactor. *PNAS* 116:16841–46
125. Oyala PH, Stich TA, Stull JA, Yu F, Pecoraro VL, Britt RD. 2014. Pulse electron paramagnetic resonance studies of the interaction of methanol with the S_2 state of the Mn_4O_5Ca cluster of photosystem II. *Biochemistry* 53:7914–28
126. Retegan M, Pantazis DA. 2016. Interaction of methanol with the oxygen-evolving complex: atomistic models, channel identification, species dependence, and mechanistic implications. *Chem. Sci.* 7:6463–76
127. Retegan M, Pantazis DA. 2017. Differences in the active site of water oxidation among photosynthetic organisms. *J. Am. Chem. Soc.* 139:14340–43
128. Kim CJ, Debus RJ. 2017. Evidence from FTIR difference spectroscopy that a substrate H_2O molecule for O_2 formation in photosystem II is provided by the Ca ion of the catalytic Mn_4CaO_5 cluster. *Biochemistry* 56:2558–70
129. Kim CJ, Debus RJ. 2019. One of the substrate waters for O_2 formation in photosystem II is provided by the water-splitting Mn_4CaO_5 cluster's Ca^{2+} ion. *Biochemistry* 58:3185–92
130. Shoji M, Isobe H, Shigeta Y, Nakajima T, Yamaguchi K. 2018. Concerted mechanism of water insertion and O_2 release during the S_4 to S_0 transition of the oxygen-evolving complex in photosystem II. *J. Phys. Chem. Lett. B* 122:6491–502
131. Krewald V, Neese F, Pantazis DA. 2019. Implications of structural heterogeneity for the electronic structure of the final oxygen-evolving intermediate in photosystem II. *J. Inorg. Biochem.* 199:110797
132. Messinger J. 2004. Evaluation of different mechanistic proposals for water oxidation in photosynthesis on the basis of Mn_4O_xCa structures for the catalytic site and spectroscopic data. *Phys. Chem. Chem. Phys.* 6:4764–71
133. McEvoy JP, Brudvig GW. 2006. Water-splitting chemistry of photosystem II. *Chem. Rev.* 106:4455–83
134. Sproviero EM, Gascón JA, McEvoy JP, Brudvig GW, Batista VS. 2008. Quantum mechanics/molecular mechanics study of the catalytic cycle of water splitting in photosystem II. *J. Am. Chem. Soc.* 130:3428–42
135. Siegbahn PEM. 2013. Water oxidation mechanism in photosystem II, including oxidations, proton release pathways, O-O bond formation and O_2 release. *Biochim. Biophys. Acta* 1827:1003–19
136. Li X, Siegbahn PEM. 2015. Alternative mechanisms for O_2 release and O-O bond formation in the oxygen evolving complex of photosystem II. *Phys. Chem. Chem. Phys.* 17:12168–74
137. Shoji M, Isobe H, Shigeta Y, Nakajima T, Yamaguchi K. 2018. Nonadiabatic one-electron transfer mechanism for the O-O bond formation in the oxygen-evolving complex of photosystem II. *Chem. Phys. Lett.* 698:138–46
138. Yamaguchi K, Shoji M, Isobe H, Yamanaka S, Kawakami T, et al. 2018. Theory of chemical bonds in metalloenzymes XXI. Possible mechanisms of water oxidation in oxygen evolving complex of photosystem II. *Mol. Phys.* 116:717–45
139. Guo Y, Li H, He L-L, Zhao D-X, Gong L-D, Yang Z-Z. 2017. The open-cubane oxo–oxyl coupling mechanism dominates photosynthetic oxygen evolution: a comprehensive DFT investigation on O–O bond formation in the S_4 state. *Phys. Chem. Chem. Phys.* 19:13909–23
140. Codola Z, Gomez L, Kleespies ST, Que L, Costas M, Lloret-Fillol J. 2015. Evidence for an oxygen evolving iron-oxo-cerium intermediate in iron-catalysed water oxidation. *Nat. Commun.* 6:5865
141. Siegbahn PEM. 2017. Nucleophilic water attack is not a possible mechanism for O–O bond formation in photosystem II. *PNAS* 114:4966–68
142. Sala X, Romero I, Rodríguez M, Escriche L, Llobet A. 2009. Molecular catalysts that oxidize water to dioxygen. *Angew. Chem. Int. Ed.* 48:2842–52

143. Blakemore JD, Crabtree RH, Brudvig GW. 2015. Molecular catalysts for water oxidation. *Chem. Rev.* 115:12974–3005
144. Nilsson H, Rappaport F, Boussac A, Messinger J. 2014. Substrate–water exchange in photosystem II is arrested before dioxygen formation. *Nat. Commun.* 54305
145. Isobe H, Shoji M, Shen J-R, Yamaguchi K. 2016. Chemical equilibrium models for the S_3 state of the oxygen-evolving complex of photosystem II. *Inorg. Chem.* 55:502–11
146. Corry TA, O'Malley PJ. 2018. Evidence of O—O bond formation in the final metastable S_3 state of nature's water oxidizing complex implying a novel mechanism of water oxidation. *J. Phys. Chem. Lett.* 9:6269–74
147. Renger G. 1978. Theoretical studies about the structural and functional organization of the photosynthetic oxygen evolution. In *Photosynthetic Oxygen Evolution*, pp. 229–48. London: Academic
148. Zhang BB, Sun LC. 2018. Why nature chose the Mn_4CaO_5 cluster as water-splitting catalyst in photosystem II: a new hypothesis for the mechanism of O-O bond formation. *Dalton Trans.* 47:14381–87
149. Dilbeck PL, Hwang HJ, Zaharieva I, Gerencser L, Dau H, Burnap RL. 2012. The D1-D61N mutation in *Synechocystis* sp PCC 6803 allows the observation of pH-sensitive intermediates in the formation and release of O_2 from photosystem II. *Biochemistry* 51:1079–91
150. Bao H, Burnap RL. 2015. Structural rearrangements preceding dioxygen formation by the water oxidation complex of photosystem II. *PNAS* 112:6139–47
151. Kim CJ, Bao H, Burnap RL, Debus RJ. 2018. Impact of D1-V185 on the water molecules that facilitate O_2 formation by the catalytic Mn_4CaO_5 cluster in photosystem II. *Biochemistry* 57:4299–311
152. Loll B, Kern J, Saenger W, Zouni A, Biesiadka J. 2005. Towards complete cofactor arrangement in the 3.0 Å resolution structure of photosystem II. *Nature* 438:1040–44
153. Guskov A, Kern J, Gabdulkhakov A, Broser M, Zouni A, Saenger W. 2009. Cyanobacterial photosystem II at 2.9-Å resolution and the role of quinones, lipids, channels and chloride. *Nat. Struct. Mol. Biol.* 16:334–42
154. Zimmermann JL, Rutherford AW. 1984. EPR studies of the oxygen-evolving enzyme of photosystem II. *Biochim. Biophys. Acta* 767:160–67
155. Cox N, Rapatskiy L, Su J-H, Pantazis DA, Sugiura M, et al. 2011. Effect of Ca^{2+}/Sr^{2+} substitution on the electronic structure of the oxygen-evolving complex of photosystem II: a combined multifrequency EPR, ^{55}Mn-ENDOR, and DFT study of the S_2 state. *J. Am. Chem. Soc.* 133:3635–48
156. Hillier W, Messinger J, Wydrzynski T. 1998. Substrate water ^{18}O exchange kinetics in the S_2 state of photosystem II. In *Photosynthesis: Mechanisms and Effects*, ed. G Garab, pp. 1307–10. Dordrecht, Neth.: Springer